

Filtered Partial Differential Equations: a robust surrogate constraint in physics-informed deep learning framework

Dashan Zhang^a, Yuntian Chen ^{*b}, and Shiyi Chen ^{†b, a}

^aDepartment of Mechanics and Aerospace Engineering, Southern University of Science and Technology, Shenzhen 518055, China

^bNingbo Institute of Digital Twin, Eastern Institute of Technology, Ningbo 315200, China

Abstract

Embedding physical knowledge into neural network (NN) training has been a hot topic. However, when facing the complex real-world, most of the existing methods still strongly rely on the quantity and quality of observation data. Furthermore, the neural networks often struggle to converge when the solution to the real equation is very complex. Inspired by large eddy simulation (LES) in computational fluid dynamics, we propose an improved method based on filtering. We analyzed the causes of the difficulties in physics informed machine learning, and proposed a surrogate constraint (filtered PDE, FPDE in short) of the original physical equations to reduce the influence of noisy and sparse observation data. In the noise and sparsity experiment, the proposed FPDE models (which are optimized by FPDE constraints) have better robustness than the conventional PDE models. Experiments demonstrate that the FPDE model can obtain the same quality solution with 100% higher noise and 12% quantity of observation data of the baseline. Besides, two groups of real measurement data are used to show the FPDE improvements in real cases. The final results show that FPDE still gives more physically reasonable solutions when facing the incomplete equation problem and the extremely sparse and high-noise conditions. The proposed FPDE constraint is helpful for merging real-world experiment data into physics-informed training, and it works effectively in two real-world experiments: simulating cell movement in scratches and blood velocity in vessels.

Keywords: Filtered equations, Physics informed, Low-quality observation, Data restoration.

1 Introduction

One of the most effective techniques for fitting an unknown data distribution is deep learning. As background information, a brief introduction to the physics-informed framework is provided in this section. This framework utilizes the governing equation to better solve problems and increase the model's performance. Meanwhile, we demonstrate the challenge inherent in this framework with some examples. Due to the complexity of the original equations, the optimization of the neural network becomes difficult. Therefore, the idea of simplifying the issue via surrogate equations is brought forward. Correspondingly, this improvement can lessen the reliance on the quality and quantity of data in physics-informed training.

1.1 Background of solving PDE via NN

Since the advent of scientific inquiry, scholars have endeavored to formulate and resolve equations to elucidate natural phenomena. Differential equations, which contain derivatives of unknown variables, represent a cornerstone of both physical and mathematical discourse. For a large number of partial differential equation (PDE) systems, it is challenging to directly obtain their analytical solutions. Therefore,

*Corresponding author: ychen@eitech.edu.cn

†Corresponding author: chensy@sustech.edu.cn

numerous numerical methods have been developed and employed to approximate the solutions of PDEs through simulation.

With the development of artificial intelligence, data-driven models are widely used in many disciplines [1, 2, 3, 4]. The Neural network (NN) models show their strong fitting ability in Computer vision (CV, [5]) and Natural language processing (NLP, [6]) field. In the field of engineering computation, the Fourier neural operator (FNO) is proposed to learn the features in Spectral space [7]; deconvolutional artificial neural network (DANN) is developed for subgrid-scale (SGS) stress in large eddy simulation (LES) of turbulence [8]; generative adversarial network (GAN) is also used to generate complex turbulence under the condition of missing data due to its good fidelity [9]. The inherent abstract reasoning process of neural networks (NNs) empowers them to adeptly learn embedding mappings across a wide array of training datasets. With the gradient descent [10] method, the NN can learn the pattern, which is the relationship of different features from the data in the optimization process. Many kinds of NN architecture are raised, such as the convolutional block [11] and the self-attention block [12], to treat different features. But when the data is insufficient to cover the features in embedding space, the question arises: can domain knowledge be incorporated to enhance the optimization process?

The paradigms that add equation constraints into the optimization process of NN, such as the physics-informed neural network (PINN, [13]), provide a beautiful vision of solving PDE with domain knowledge automatically. Training models with explicit physical constraints, such as the incorporation of governing equations, has shown promise in yielding improved results. Over the past four years, there has been a notable surge in the utilization of physics-informed methods across diverse domains. In the physics-informed based problem, some scientific machine learning frameworks are proposed (e.g., the DeepXDE, [14]; AutoKE, [15]; the NeuroDiffEq, [16] framework) to solve the differential equations. In the inverse problem of physics-informed learning, the model is built for the equation discovering. Scholars have proposed many methods that can work in the knowledge discovery field [17], the sparse regression method is capable of discovering the PDEs in given system [18]; the deep learning has also been proved to be effective on the physics-informed inverse problem (e.g., the DL-PDE, [19]); the symbolic genetic algorithm (SGA-PDE) can be used to discover the open-form PDEs [20]; based on the Reynolds-averaged Navier–Stokes (RANS) equations, the physics-informed model is used to improve turbulence models [21]. In the evaluation of PINN, PINN has been shown to be robust against the influence of sparsity and noise levels in training data [22], but its accuracy diminishes beyond the training time horizon [23]. In short, physics-informed model is generally considered as a modeling tool, particularly in contexts such as turbulence modeling, which have been demonstrated in isolated scenarios [24].

In the view of application, physics-informed framework has improved the model performance in many scenarios: using the physical laws in power systems, NN can model the power system behavior both in steady-state and in dynamics [25]; the theory-guided deep-learning load forecasting (TgDLF) model the future load through load ratio decomposition with the considered historical load, weather forecast and calendar effect [26]; digital twins have been widely mentioned as an important preface application, highlighting the significance of modeling with physical constraints for their implementation [27]; in the subgrid modelling of Kraichnan turbulence, the data-driven method can predict the turbulence source term through localized grid-resolved information [28]; with acoustic wave equation, NN can identify and characterize a surface breaking crack in a metal plate [29]; with the advection-diffusion equations, NN can obtain better super-resolution outputs in the images of atmospheric pollution [30]; through the PINN-based method, three-dimensional Tomographic Background Oriented Schlieren imaging fields, such as the temperature field of an espresso cup, can be rapidly modeled [31]; using two-dimensional three-component stereo particle-image velocimetry (PIV) datasets, PINN demonstrates the capability to reconstruct the mean velocity field and correct measurement errors ([32], [33]); based on stochastic particle advection velocimetry (SPAV) data, the PINN approach significantly improves the accuracy of particle tracking velocimetry reconstructions [34]; in the field of geophysics, NN have shown enhanced ability to model the subsurface flow with the guiding of theory (e.g., governing equations, engineering controls and expert knowledge, [35]).

Unlike the numerical simulation method, the universal approximation theorem shows that a NN is able to approximate any continuous function on a compact subset of \mathcal{R}_n with sufficient precision when it has enough parameters [36]. Considering that the optimization process of NN can be summarized as ‘finding the parameters to minimize the given loss function’, the equations can be added into the loss function to make NN solve PDE automatically. When facing a complex problem, adding some simulation or measurement data points to help NN determine the large-scale distribution of solutions is a common method. Subsequently, we refer to these data points as ‘observation points’.

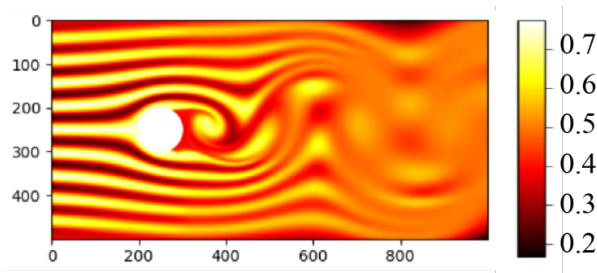


Fig. 1. The fluid flow through a cylinder wall (streak-lines). To keep the consistency of data, the reference simulation solutions are from the open-resource data of Hidden fluid mechanics, HFM [41]

Regarding solving equations, the Navier-Stokes [37] equation (equation(s) 1) in fluid mechanics is one of the most challenging problems. Both exact solutions [38] and computer simulations [39] play important roles in theory and engineering. When it comes to physics-informed training in fluid fields, modeling with the constraint of N-S equations is one of the most common methods.

$$\frac{\partial u}{\partial t} + u \cdot \nabla u = -\frac{1}{\rho} \nabla p + \nu \nabla^2 u \quad (1)$$

$$\nabla \cdot u = 0 \quad (2)$$

where u, p, ρ, ν represent the velocity vector, pressure, density and dynamic viscosity, respectively.

In this paper, we utilize cylinder flow as an illustrative example to elucidate the challenges encountered in physics-informed training. We introduce our enhanced methodology and validate its effectiveness across diverse scenarios. The cylinder flow, governed by the N-S equation, is a classic example which can reflect the properties of the fluid [40]. In the cylinder flow case, the boundary condition (BC) describes a cylinder wall in the flow field generally. In equation(s) 3, the velocity u is limited to zero on the surface of the cylinder wall, where r is the radius of the cylinder wall. The simulation solution reflects the flow in figure 1.

$$u(r \cdot \cos\theta, r \cdot \sin\theta) = (0, 0), \theta \in [0, 2\pi] \quad (3)$$

In recent years, many scholars have employed NN to address both the direct and inverse problems associated with cylinder flow. Though it is an under-determined problem, the velocity field restoration from concentration field is solved effectively by NN [41]. In the knowledge discovery field, NN can abstract the N-S equation from the velocity field of cylinder flow with high precision [18]. To a certain extent, these works show that NN can describe the solution of the N-S equation. However, current researches heavily relies on the quality and quantity of observation data, thus training based on low quality (i.e., noisy and sparse) data is still an open question.

In general, using physical constraints to improve the NN modeling ability of observation data is a powerful method. However, this approach necessitates high-quality and abundant data. When it comes to the modeling of real measurement data, it becomes crucial to effectively model the sparse and noisy data.

1.2 Current challenges

Obtaining a satisfactory approximate solution solely through PDE constraints can be particularly challenging. The optimization problem of NN is always a non-convex due to the non-linear part inside (optimization of a single hidden-layer NN with non-linear activation function has been proved to be a non-convex problem, [42]). Finding the optimal solution with a gradient-based method is NP-hard because the problem is non-convex. As a result, the majority of constructive works typically rely on utilizing more informative data during training (e.g., the observation data of concentration in the full domain on HFM, [41]).

According to the relationship between the observation and the test domain, the physics informed problem can be divided into three different tasks (as shown in figure 2). When the observation points all locate outside the desired interval (red test domain in figure 2), the task of the NN is essentially extrapolation (figure 2.a). When the observation points are sampled in the same interval of the test

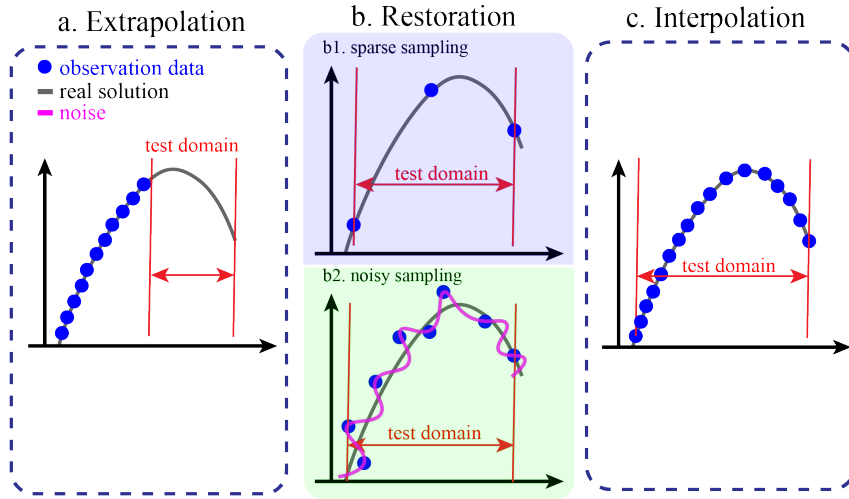


Fig. 2. Summary of the physics-informed training tasks. (a) The extrapolation, where known and unknown parts conform to the different data distributions. NN is trained to learn the hidden pattern in the known part, and extrapolate it in the unknown part. (b) The restoration, of which the given and unknown parts conform to the same data distribution. Meanwhile, the data has poor quality and quantity. b1 shows the restoration from sparse data, and b2 is the restoration from noisy data. (c) sufficient and accurate data with the same distribution, which makes the task an ordinary interpolation problem.

domain, the task is called restoration if the observation data is noisy or sparsely sampled from the observation points (see figure 2.b), or interpolation if the data is abundant and accurate (see figure 2.c).

In this paper, we focus on the restoration task (i.e., figure 2.b) since it is more commonly encountered in practice. The NN is designed to learn the embedding distribution of solutions with noisy and sparse data. With the help of physical constraints, NN can provide more reasonable and accurate modeling results. The meaning of restoration is finding a better method to model the noisy and sparse data in the real experiment. The quantity and quality of data required for modeling can be greatly reduced, resulting in lower costs in practice.

As the complexity of the problem increases, a greater amount of observation data is required to describe the distribution of the exact solution. In figure 3, the first example of Burgers equation (figure 3.a) shows NN giving the incorrect solution in the interval with the larger differential term. Solutions of different viscosities show the effect of regularity in PDE solutions, which makes NN tend to give smoother outputs. The second example (figure 3.b), a simple exponential function, directly shows that even though the equation is infinitely differentiable, NN performs poorly when there is a magnitude gap between the scale of the differential terms. The last example is the cylinder flow (figure 3.c) under the large Reynolds number (Re) condition, the complex velocity field makes NN converge to a trivial solution. The frequent alterations in velocity impede the NN's ability to learn the embedding pattern effectively, leading it to merely yield the mean value to attain a local optimum.

To summarize, the more complex the problem, the greater the amount of data required for training. The sparse and noisy data still contain limited information about the solution's distribution. However, much of the missing information can be inferred by leveraging the PDE as domain knowledge. Although NN can infer most of the missing value, the observation data is still indispensable because it acts as the fixed points in outputs, which anchor the large-scale solutions. The main area for improvement is how to use less or noisier observation data to train a more robust NN. More specifically, the current challenges of physics-informed training can be itemized as follows:

- The experiment always produces sparse quantities of data when the observation points are gathered through measurements. Lack of data causes NN solutions to frequently yield trivial solutions in complex problems (e.g., figure 3.c).
- The measurement noise makes observation data out of line with the underlying governing equations. The noise in observation (especially at initial points) can seriously affect the NN optimization process.

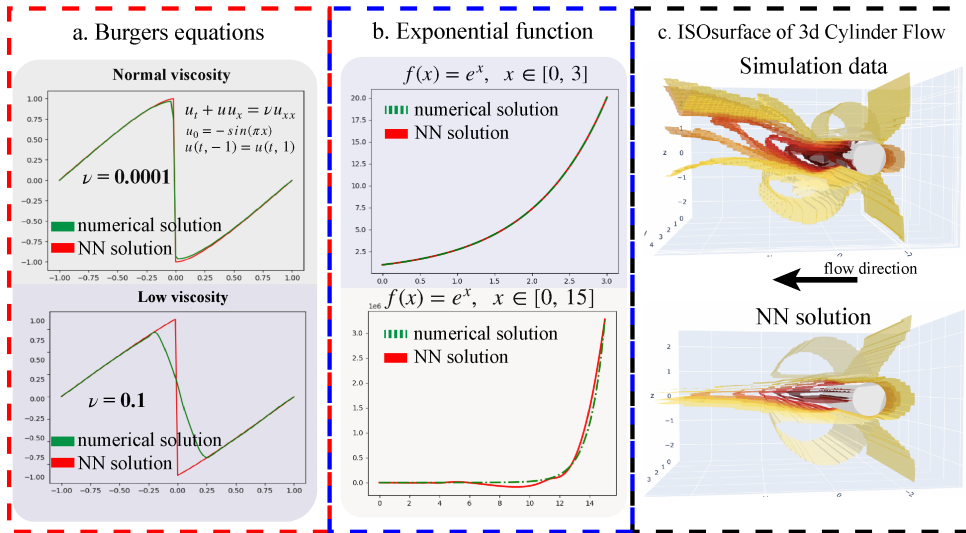


Fig. 3. The NN output guided by different equations. (a) The Burgers equation is the classic example in PINN [13], which is used to show the effect of regularity; (b) The exponential function, which shows the difficulty of NN to handle the interval with a small loss value. NN always focus on the large loss interval; (c) The N-S equation. Facing the complex solution, NN is tend to be trapped in the local minimum and obtain the trivial solution.

In order to abstract more information from low-quality and low-quantity data, the equation constraints are improved. In this paper, we propose a new surrogate constraint for the conventional PDE loss using deep learning and numerical method filtering. The surrogate constraint takes the advantage of the mesh-less feature of NN, calculates the PDE loss with the filtered variables instead of the original PDE. The proposed method can be regarded as an intermediary layer based on filter operations, which maintains the equation’s form, and is unaffected by the NN architecture. Our proposed filtered PDE model (referred to as FPDE) in this paper shows the following contributions:

- The study proposes a filtered PDE framework that is inspired by large eddy simulation (LES). The solution of physics-informed training is more robust under the constraints of the proposed framework.
- In the noise experiments, the FPDE model can obtain the same quality solution with 100% higher noise than the baseline.
- In the sparsity experiments, the FPDE model can obtain the same quality solution with only 12% quantity of observation points of baseline.
- In the real-world experiments with missing equations, the FPDE model can obtain a more physically reasonable solution.

In essence, using FPDE as surrogate constraints significantly enhances the ability of neural networks to model data distributions, particularly when dealing with noisy and sparse observations. This improvement is considerable, especially for the work relying on experimental data.

2 The motivation and ‘conflict’ theory

To enhance the modeling of noisy and sparse data, a promising avenue for improvement is the co-optimization between PDE and data loss. We discovered that the discrepancy between the directions of the PDE loss and the data loss contributes to some of the challenges in NN optimization. In this paper, the aforementioned challenge is defined as ‘conflict’ and its mathematical derivation is provided and discussed. To mitigate the impact of this conflict, we introduce an improved method inspired by a classic numerical approach (i.e., large eddy simulation, [43]). In this part, the incompressible N-S equation is used as an example for demonstration.

2.1 Mechanism of ‘conflict’

The deep neural network, usually optimized by the gradient-based method, provides a solving paradigm with a large number of parameters. With the classic loss function (i.e., mean squared error, MSE), the solving PDE by NN can be described as a soft-constraint method. Different from the hard-constraint numerical method, the soft-constraint method doesn’t constrain the calculation in each step, but only optimizes the final solution by loss function [26]. Under the soft constraint, the optimization process of the parameters in NN is essential. The challenges within the physics-informed framework can be explained from the perspective of optimization.

In the physics-informed framework, the loss function can be written as equation(s) 4. The IC/BC loss is determined by the initial and boundary conditions, while the PDE loss is computed using the collocation points, which are specific points solely utilized for PDE calculation and remain independent of the observation data distribution. Given the PDE, initial, and boundary conditions, and the observation data jointly determining the final loss, NN training can be broadly defined as the co-optimization of these losses.

During the co-optimization process, the weighting factors assigned to loss terms are crucial hyperparameters. These weights are influenced by factors such as the dataset, neural network architecture, and other hyperparameters, and therefore, the optimal weights may vary accordingly. Consequently, the tuning of hyperparameters becomes necessary. Numerous studies have highlighted the significance of weight tuning in training PINN. [44] present a potential solution for hyperparameter tuning, and the underlying mechanism is described in [45]. Furthermore, [46] provide a comprehensive review of PINN development and emphasize that hyperparameters, such as the learning rate and number of iterations, can enhance generalization performance. In the context of tuning multiple regularization terms, [47] propose an optimization method based on Lagrangian dual approaches. However, in this particular work, our primary focus lies on quantitatively improving conventional PINN using the proposed method. Therefore, the weights in equation(s) 4 are uniformly set to 1, which is a commonly adopted setting in several studies (e.g., [41], [48], and [49]).

$$Loss = L_{data} + \omega_1 L_{PDE} + \omega_2 L_{ICBC} \quad (4)$$

where $L_{data} = \frac{1}{N} \|y - \hat{y}\|_2$ and $L_{PDE} = \frac{1}{M} \|residual\ PDE\|_2$. The L_{ICBC} is decided on the task specifically. y and \hat{y} represent the NN output and observation respectively. ω_1 and ω_2 represent the weights of PDE loss and ICBC loss.

The optimization direction of the model is the gradient direction of parameters update. It is jointly determined by the sum of each loss direction during each iteration of the multi-objective optimization in equation(s) 4. The direction of the loss functions in one optimization step can be written as the partial derivative terms in equation(s) 5, which shows the effect of the loss function on the parameters of NN.

$$\theta_t = \theta_{t-1} - \eta \left(\frac{\partial L_{data}}{\partial \theta_{t-1}} + \frac{\partial L_{pde}}{\partial \theta_{t-1}} + \frac{\partial L_{ICBC}}{\partial \theta_{t-1}} \right) \quad (5)$$

where θ_t represents the NN parameters in iteration t and η represents the learning rate (defined as hyperparameter in advance).

Theoretically, there must exist a group of parameters that make PDE and data loss all close to 0. The closed PDEs have embedding distributions of the solutions, but the distribution may have complex pattern, including high-frequency features that pose challenges for neural network (NN) learning. Meanwhile, the observation data also maps the distribution of exact solutions. The physics-informed framework enables NN to learn both the intricate high-frequency patterns from the PDE constraint and the large-scale distribution from observation data. Therefore, having the same embedding distribution under different constraints is the premise of co-optimization.

In the ideal physics-informed framework, PDE and data constraints can help each other out of the local optimum. But in fact, the relationship between these two losses backfired in many practical problems. In the training of physics-informed task, the optimized function is always the residual form of the governing equations, which is the difference between the left and right hand sides of the equation. The 2-dimensional N-S equations are used (2-d case of equation(s) 1) as the example to demonstrate the conflict in the co-

optimization process. The PDE and data loss can be written in a 2-dimensional case as:

$$\begin{aligned}
L_{PDE} &= \frac{1}{M} \left\| \frac{\partial u_i}{\partial t} + u_j \frac{\partial u_i}{\partial x_j} + \frac{1}{\rho} \frac{\partial p}{\partial x_i} - \nu \frac{\partial^2 u_i}{\partial x_j^2} \right\|_2 + \frac{1}{M} \left\| \frac{\partial u_i}{\partial x_i} \right\|_2 \\
&= \frac{1}{M} \left\| \frac{\partial u}{\partial t} + \left(u \frac{\partial u}{\partial x} + v \frac{\partial u}{\partial y} \right) + \frac{1}{\rho} \frac{\partial p}{\partial x} - \nu \left(\frac{\partial^2 u}{\partial x^2} + \frac{\partial^2 u}{\partial y^2} \right) \right\|_2 \\
&\quad + \frac{1}{M} \left\| \frac{\partial v}{\partial t} + \left(u \frac{\partial v}{\partial x} + v \frac{\partial v}{\partial y} \right) + \frac{1}{\rho} \frac{\partial p}{\partial y} - \nu \left(\frac{\partial^2 v}{\partial x^2} + \frac{\partial^2 v}{\partial y^2} \right) \right\|_2 \\
&\quad + \frac{1}{M} \left\| \frac{\partial u}{\partial x} + \frac{\partial v}{\partial y} \right\|_2 \\
L_{data} &= \frac{1}{N} \left\| \mathbf{y} - \hat{\mathbf{y}} \right\|_2
\end{aligned} \tag{6}$$

where $\mathbf{x} = (t, x_i) = (t, x, y)$ and $\mathbf{y} = (u_i, p) = (u, v, p)$ represent the input and output of NN respectively. M and N are the number of collocation points and observation points.

Since the discrete data also contains the differential information, observation data adds the embedding PDE information to the training process. When the data is sufficient and clean (as in the situation in figure 2.c), the observation data is consistent with PDE constraints. The PDE can be represented by observation data as proposition 1.

Proposition. 1. *The no conflict condition. When the number and distribution of observation data are sufficient to describe PDE solutions and the observation data is accurate, discrete data satisfy PDE constraints. The conflict can be represented as the following equation (the difference between residual form of PDE and observation data). In this condition, the conflict is close to 0.*

$$PDE(\mathbf{y}) = \frac{u_i^{t+1} - u_i^t}{\Delta t} + u_j \frac{u_i^{x_j+1} - u_i^{x_j}}{\Delta x_j} + \frac{1}{\rho} \frac{p^{x_i+1} - p^{x_i}}{\Delta x_i} - \nu \frac{u_i^{x_j+1} - 2u_i^{x_j} + u_i^{x_j-1}}{\Delta x_j^2} \approx 0$$

where $PDE(\mathbf{y})$ is the residual form value of given PDE. The variables in proposition 1 all from the observation data.

When the data is noisy (like the restoration in figure 2.b2), the observation data inherently incorporates noisy information regarding the embedding solution distribution (given in proposition 2). That is, even if the NN can fit the observation data, the PDE constraint cannot be satisfied.

Proposition. 2. *The conflict caused by the noise in observation data. When the noisy data is used in the NN training, the conflict between PDE and data constraints occurs. The noisy data can't represent PDE well, which makes the residual form value of PDE with noisy data larger than that with accurate data. When the NN tries to fit the value, the PDE constraint loss will increase, which causes the difficulties in co-optimization.*

$$\begin{aligned}
PDE(\mathbf{y} + \epsilon) &= \frac{(u_i^{t+1} + \epsilon) - (u_i^t + \epsilon)}{\Delta t} + (u_j + \epsilon) \frac{(u_i^{x_j+1} + \epsilon) - (u_i^{x_j} + \epsilon)}{\Delta x_j} \\
&\quad + \frac{1}{\rho} \frac{(p^{x_i+1} + \epsilon) - (p^{x_i} + \epsilon)}{\Delta x_i} - \nu \frac{(u_i^{x_j+1} + \epsilon) - 2(u_i^{x_j} + \epsilon) + (u_i^{x_j-1} + \epsilon)}{\Delta x_j^2} \\
\text{thus } \|PDE(\mathbf{y} + \epsilon)\|_2 &\geq \|PDE(\mathbf{y})\|_2 \approx 0, \quad \epsilon \sim N(0, \sigma)
\end{aligned}$$

When the observation data is sparse and incomplete, the contained information is not enough to aid NN to learn the large-scale distribution of solutions (proposition 3). Under this condition, NN needs to learn the PDE relationship at collocation points without reference. The search space of optimization will expand significantly from the standpoint of the gradient descent process. Although the observation data is error-free and the actual PDE calculation happens at the collocation points, the optimization directions of PDE and data loss (like partial derivative terms in equation(s) 5) are always in conflict.

Proposition. 3. *The conflict caused by the missing of observation data. When the training data is sparse sampled, the distribution information in observation data is not enough. NN acquire to find the missing value by PDE constraint, thus cause the potential conflict in the optimization process. Theoretically, the $PDE(\mathbf{y}_{sparse})$ can be closed to 0, but finding the correct solution is similar to solving PDE with no observation data.*

$$PDE(\mathbf{y}_{sparse}) = \frac{u_i^{T+1} - u_i^T}{\Delta T} + u_j \frac{u_i^{X_j+1} - u_i^{X_j}}{\Delta X_j} + \frac{1}{\rho} \frac{p^{X_i+1} - p^{X_i}}{\Delta X_i} - \nu \frac{u_i^{X_j+1} - 2u_i^{X_j} + u_i^{X_j-1}}{\Delta X_j^2}$$

where $\Delta T, \Delta X_i \gg \Delta t, \Delta x_i$.

The presence of inevitable conflict introduces ambiguity into the optimization direction. The conflict slows the effective gradient descent and eventually results in an insurmountable local optimum.

2.2 The inspiration from LES

In order to model the noisy and sparse data better, it is necessary to find a way to overcome the conflict. When calculating the differential terms, the influence of noise or sparsity should be minimized as much as possible. Similar challenges will also be faced in numerical simulation, thus we can refer to existing methods to overcome the challenges. The filters in the numerical method give us inspiration.

In the numerical simulation method, tackling complex equations invariably entails increased computational costs to uphold accuracy. In the computational fluid dynamics (CFD) field, as the Reynolds number increases, the flow tends to be unsteady and disorderly. Since the simulation range is from the domain scale to the smallest dissipation scale, the computational requirement grows at Re^3 rate [50]. Under the large Reynolds number condition, direct simulation is unaffordable.

In the realm of fluid dynamics, LES stands out for its efficiency in handling turbulent flows [43]. The LES methodology achieves this by substituting the small-scale details with an artificially designed subgrid-scale model, which effectively captures the essence of these scales without the need for excessive computational resources. This approach significantly reduces computational costs while preserving the integrity of the solution. Building upon this concept, our study poses a pertinent question: ‘Can a neural network, while learning the Navier-Stokes (N-S) equations, also act as a filter for variables, potentially enabling the derivation of more accurate large-scale solutions from a lesser amount of observational data, irrespective of the specific subgrid model employed?’ Our work explores this question by integrating NN into the framework of LES, aiming to leverage their filtering capabilities to enhance the solution quality with limited data.

In the problem of solving PDE via NN, the complex solutions also cause bias and insufficiency of observation data which intensify the conflicts in section 2.1. Therefore, it is intuitive to find a surrogate constraint to make the NN ignore the small-scale conflict and focus on the large-scale optimization. While it may seem natural to apply filtering operations directly to the observation data (i.e., the average pooling or the Gaussian filter in the data pre-processing), such operation, like pooling, loses information in the observation data and be hard to implement when the observation data is sparse and randomly distributed. Inspired by LES, we designed a method which filters the NN output in post-processing and rebuilds the governing equations (N-S equations as the example in equation(s) 7) rather than simply filter the observation data. The new PDE loss defined by the new governing equation acts as a surrogate constraint for the original PDE loss in the training, which is named as ‘filtered partial differential equations’ (FPDE) loss.

$$FPDE(\bar{\mathbf{y}}) = \frac{\partial \bar{u}_i}{\partial t} + \frac{\partial \bar{u}_i \bar{u}_j}{\partial x_j} + \frac{1}{\rho} \frac{\partial \bar{p}}{\partial x_i} - \nu \frac{\partial^2 \bar{u}_i}{\partial x_j^2} \quad (7)$$

3 Methodology

To deploy the filter before the PDE calculation, a new intermediate layer is designed to connect the normal NN outputs and the differentiation module. The proposed layer can be regarded as an explicitly defined layer according to the given equation, which connected after the output layer and dedicated to the computation of differential terms. It facilitates the calculation smooth the small-scale oscillations. In addition to the theoretical analysis (section 3.2), three experiments are conducted to verify the proposed method. The sparsely sampled simulation data with artificial noise is used to evaluate the improvement quantitatively, followed by testing with the real cell migration and arterial flow data.

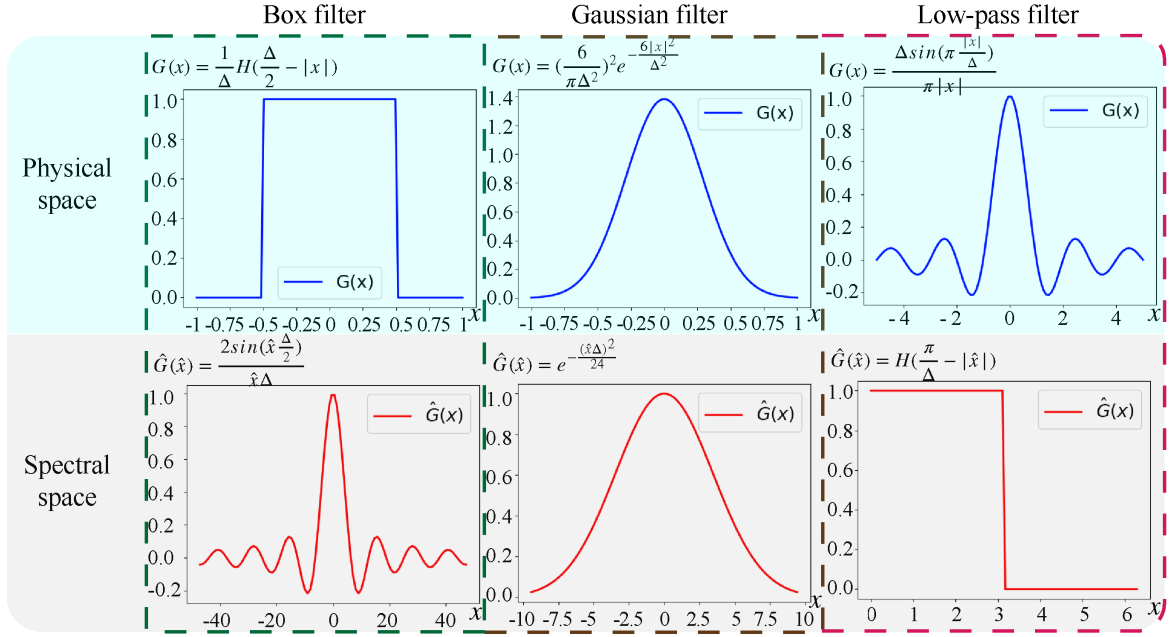


Fig. 4. The classic filters in physical and spectral space. The most common Gaussian weight filter kernel will be used in subsequent experiments.

3.1 Deploying filter after NN inference

The filter operation in physics always implies the constraint of spatial resolution, which can be defined as the convolutional integral in equation(s) 8. In this integral equation, G is the filter, and ϕ is the objective function.

$$\bar{\phi}(x, t) = \int_{-\infty}^{\infty} \phi(y, t)G(x - y)dy \quad (8)$$

The classic physical isotropic spatial filters (G in equation(s) 8) and its Fourier transformation in spectral space is shown in figure 4 [51]. All filters satisfy the normalization condition to maintain the constants, and the kernel size of filters is represented as Δ . In this paper, all the experiments used the Gaussian kernel. The subsequent experiment verified that the FPDE results are not significantly affected by the type of filter. For details and results of the experiment, please refer to appendix A.

In the context of the computer vision, the filter operation on data is usually called down sampling. When the filter is applied to the PDE calculation, it can be viewed as a new layer in the NN and builds the bridge between the ‘fully connected layer’ and ‘auto differentiation’ (shown in figure 5).

The primary distinction between the regular model and the FPDE model is the calculation of PDE. A multi-layer fully connected network is used as the body. The inputs of NN are the coordinates x and the time t . The unknown variables in PDE are the NN outputs (N-S equations as example in figure 5). In figure 5.b, the conventional process for calculating the PDE loss is depicted, wherein the differential terms are directly obtained from the NN outputs via auto differentiation. The improvements in FPDE are shown in figure 5.c: (1) In the orange box, the cross-terms in the N-S equations are calculated before the filter operation. The cross-terms are necessary since the filter operation does not satisfy the associative property of multiplication. Because of the filter operation, the product of two filtered variables is not equal to the filtered result of the product of two variables. (2) The proposed filter, or the defined new activation layer, is shown in the green box. Benefiting from the mesh-free feature of NN, the gridded outputs for the filter operation can be obtained. The u is filtered to \bar{u} by the Gaussian kernel, and the differential terms are calculated on the filtered outputs. Figure 5.d is the calculation of equation constraints. Conventional PINN will use the original outputs to calculate the differential term, while the FPDE will use the filtered outputs. In the calculating of residual form of N-S equations, the Reynolds number of the training data, provided initially, is incorporated into the viscosity term.

In the training of the N-S equations case, a multi-layer NN with residual connections is used. The hidden layer of the NN has three paths with depths of 1, 4, and 16 blocks. The results of these three paths

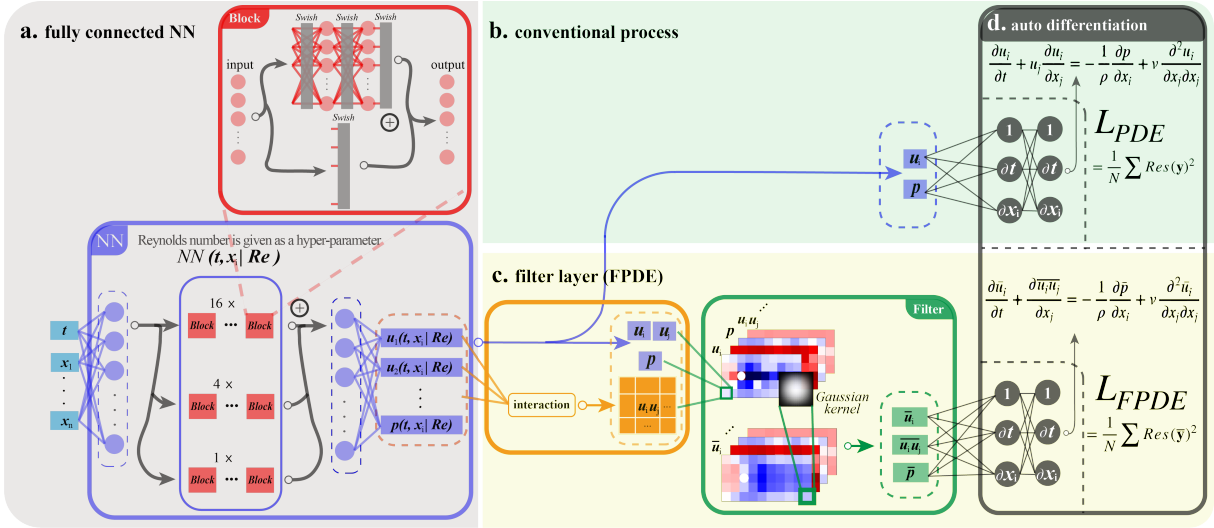


Fig. 5. The physics-informed training framework and the proposed FPDE method. The example of solving the N-S equation governed problem. (a) The fully connected neural network. A NN with multiple residual connections is used to model the observation. (b) The conventional PDE loss calculation process, which uses NN outputs in differentiation directly. (c) The improved framework in the PDE loss calculation iteration. The orange part is used to calculate the cross-terms in the equations; the green part is used to filter all variables. The PDEs are calculated with filtered variables instead. (d) The auto differentiation part. Derivatives are automatically generated from the computational graph.

are summed before entering the output layer. Each block consists of 3-layer deep NN with 20 neurons per hidden layer and one residual connection (shown in red box, figure 5.a). The activation functions in this NN are all Swish functions.

The details of the training process for FPDE and the conventional PDE model can be summarized in Table.1.

The algorithm 1 is the description of figure 5. Algorithm 1 compares the difference between the FPDE and classical model more clearly. In both models, the form of the governing equations, initial and boundary conditions, and observation points are completely the same. The sole distinction lies in the FPDE intermediate layer between the forward propagation and auto differentiation parts, as depicted by the orange and green boxes in figure 5.b. In order to calculate the filtered PDE, the obtained NN inference outputs need to be gridded. The gridded outputs (i.e., $(\hat{u}_{col}, \hat{v}_{col}, \hat{p}_{col})$, 2-d case) are filtered by the given kernel at step 2.3. The filtered variables (i.e., $(\bar{u}_{col}, \bar{v}_{col}, \bar{p}_{col})$) are pushed into the auto differentiation part to calculate the differential terms. In the whole FPDE process, the most critical steps are 2.2 and 2.3. Benefit from the mesh-less feature of NN, obtaining the gridded neighbors of given points (i.e., the $NN(x_{col} \pm \Delta x, y_{col} \pm \Delta y, t_{col})$) and acquiring the filtered results is straightforward.

In general, the calculation of FPDE loss can be divided into two steps: calculating cross-terms and filtering. FPDE is transparent for NN architectures and forms of governing equations due to its simplicity. That means FPDE can be applied to most NN architectures and different equations, not just the given example cases.

3.2 Theoretical improvements of filter

The filtered partial differential equations (FPDE) method is deployed as the surrogate constraint of the original PDE loss. The FPDE constraint helps the optimization process of NN and improves the model's performance in the 'inference-filtering-optimization' process. Owing to the intrinsic complexity of NNs, it is challenging to directly demonstrate the specific mechanisms through which FPDE exerts its influence. In this section, we aim to provide potential avenues of explanation and propose a putative mechanism that elucidates the underlying workings of FPDE within the optimization framework of NNs.

FPDE and PDE training process (2-d NS equation as an example).

Input: Observation points $(x, y, t) \rightarrow (u, v, p)$; Collocation points $(x_{col}, y_{col}, t_{col})$.

Constraint: 2-d N-S equations ; Initial condition (IC) ; Boundary condition (BC).

Loss: Mean Squared Error (MSE) loss

Repeat:

Step 1. Data loss: for (x, y, t) in observation data

1.1. Get NN output $(\hat{u}, \hat{v}, \hat{p})$ by forward propagation.

1.2. Calculate data loss $MSE((u, v, p), (\hat{u}, \hat{v}, \hat{p}))$, both methods get data loss on the unfiltered field.

Step 2. FPDE / PDE loss: for $(x_{col}, y_{col}, t_{col})$ in collocation points

2.1. Get NN output $(\hat{u}_{col}, \hat{v}_{col}, \hat{p}_{col})$ by forward propagation.

FPDE:

2.2. Get the gridded outputs to the 2-d tensor.

2.3. Filter the 2-d tensor (convolution with Gaussian kernel, i.e., $\bar{u} = \frac{1}{\sum \omega_i} \sum_{i=1}^n \omega_i u_i$, ω_i is the weight in kernel), get the filtered $(\bar{u}_{col}, \bar{v}_{col}, \bar{p}_{col})$.

2.4. Calculate the differential terms $\frac{\partial \bar{u}_{col}}{\partial t} \dots$, etc

2.5. Calculate FPDE loss of the residual form equations.

PDE:

2.2. Calculate the differential terms $\frac{\partial u_{col}}{\partial t} \dots$, etc

2.3. Calculate PDE loss of the residual form equations.

Step 3. IC / BC loss: for $(u_{ICBC}, v_{ICBC}, p_{ICBC})$ generated by initial / boundary condition

3.1. Get NN output $(\hat{u}_{ICBC}, \hat{v}_{ICBC}, \hat{p}_{ICBC})$ by forward propagation.

3.2. Calculate IC/BC loss $MSE((u, v, p), (\hat{u}_{ICBC}, \hat{v}_{ICBC}, \hat{p}_{ICBC}))$.

Step 4. Optimization:

4.1. Calculate total loss = data loss + equation loss + IC/BC loss

4.2. Backward propagation and update NN parameters.

Until the training loss has converged.

Table 1: The FPDE algorithm and comparison with the conventional algorithm.

3.2.1 Improvements in problems with the noisy data

Training with noisy data (like the restoration in figure 2.b2), the FPDE shows increased accuracy owing to the anti-noise ability of the filter operation. As the basic filter with the Gaussian kernel, the filtered output has a smaller variance than the original output, according to the Chebyshev's inequality [52]. To illustrate this, we utilize normally distributed noise, $N(0, \sigma)$, which is a commonly used unbiased noise. After the application of the filtering process, the FPDE utilizes data with reduced noise levels compared to the original, pre-filtered data.

$$FPDE(\bar{\mathbf{y}} + \bar{\epsilon}) = \frac{(\overline{u_i^{t+1} + \epsilon}) - (\overline{u_i^t + \epsilon})}{\Delta t} + \frac{\partial(\overline{u_i + \epsilon})(\overline{u_j + \epsilon})}{\partial x_j} + \frac{1}{\rho} \frac{(\overline{p^{x_i+1} + \epsilon}) - (\overline{p^{x_i} + \epsilon})}{\Delta x_i} - \nu \frac{(\overline{u_i^{x_j+1} + \epsilon}) - 2(\overline{u_i^{x_j} + \epsilon}) + (\overline{u_i^{x_j-1} + \epsilon})}{\Delta x_j^2} \quad (9)$$

where ϵ and $\bar{\epsilon}$ represent the noise and filtered noise ($\epsilon \sim N(0, \sigma)$, $\bar{\epsilon} \sim N\left(0, \frac{\sigma \sum \omega_i^2}{\sum \omega_i}\right)$), ω_i represents the weight in filter ($\omega_i = \frac{1}{\sqrt{2\pi}} \exp(-\frac{x^2}{2})$). With the Gaussian kernel as the filter operator, the variance of noise decreases at the rate of n^{-1} (n is the size of given Gaussian kernel). This indicates that just a small kernel can greatly reduce the interference of noise.

Observational data contaminated with noise can significantly diminish the precision of predictions generated by neural networks (NNs). The effects and directional trends of such noise are illustrated in figure 6.a, where it is evident that data degradation progressively aligns the NN's output with the noisy data set during each iterative cycle. This compromised output, subsequently influenced by the noise, can introduce bias into the computation of PDEs.

Figure 6.b presents a straightforward example, demonstrating that the output refined through a filtering process (represented by the blue star) more closely approximates the actual solution. This refined

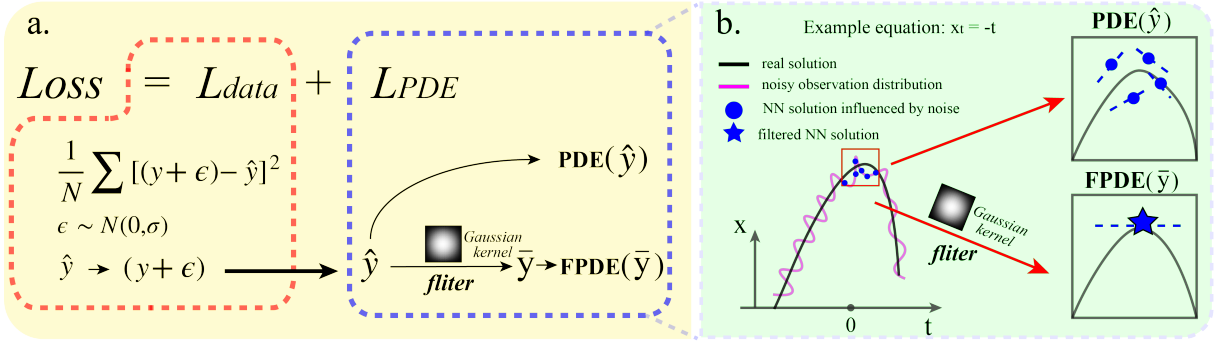


Fig. 6. Given possible mechanism of the FPDE method for processing noisy data. (a) Though the noisy data doesn't directly participate in the PDE loss calculation, it still affects the PDE loss by changing the NN output from the previous iteration. (b) The filtered NN outputs reduce the noise, making PDE calculations more robust and accurate.

output point yields an accurate derivative, which is instrumental in mitigating the NN's susceptibility to noise. In contrast, outputs from a standard PDE model (depicted as blue dots) are subject to the distorting effects of noise (represented by the pink line), thereby failing to furnish the correct derivatives necessary for precise calculations.

In summary, the implementation of a filtering mechanism effectively diminishes the magnitude of noise interference. As a result, FPDE are capable of yielding superior modeling outcomes even when the input data are noisy. It is hypothesized that the enhanced accuracy in the computation of differential terms is attributable to the reduced presence of noise within the filtered data set.

3.2.2 Improvements in problems with the sparse data

In the context of sparse data problems, the enhancement brought by FPDE can be viewed as an inverse application of the aforementioned mechanism. Within equation(s) 9, the discrepancy in the optimization trajectory between the dataset and the PDE loss is mitigated through a filtering process. This intervention allows the NN to function without being impeded by the interplay of these two forms of loss. In section 2.1, it is hypothesized that the source of discord stems from the suboptimal quality of the input data. Empirical findings indicate that the FPDE approach persists in its optimization endeavors despite heightened conflict when training with sparse data. From a co-optimization perspective, the attenuation of this conflict can be interpreted as an inverse decoupling of the data and PDE loss elements.

In comparing the FPDE model with the conventional PDE model, particularly with respect to sparse data scenarios, the PDE loss takes a straightforward residual form that directly constrains the solution. Conversely, the FPDE model operates on the filtered 'mean' solution, as detailed in equation(s) 10. Relative to the original problem, the FPDE-governed problem introduces additional variables that can be autonomously learned. When computing the equation's residual, the FPDE approach involves a greater number of NN inference outputs. Essentially, this allows for a broader spectrum of NN output values corresponding to the same filtered outcome, suggesting a richer set of potential solutions. From this vantage point, the FPDE effectively moderates the coupling between the PDE loss and data loss throughout the training process.

$$\begin{aligned}
 FPDE(\overline{\mathbf{y}_{sparse}}) &= \frac{\overline{u_i^{T+1}} - \overline{u_i^T}}{\Delta T} + \frac{\partial \overline{u_i u_j}}{\partial X_j} + \frac{1}{\rho} \frac{\overline{p^{X_i+1}} - \overline{p^{X_i}}}{\Delta X_i} - \nu \frac{\overline{u_i^{X_j+1}} - 2\overline{u_i^{X_j}} + \overline{u_i^{X_j-1}}}{\Delta X_j^2} \\
 \bar{u} &= \frac{1}{\sum \omega_i} \sum_{i=1}^n \omega_i u_i, \quad \omega_i = \frac{1}{\sqrt{2\pi}} \exp\left(-\frac{x^2}{2}\right)
 \end{aligned} \tag{10}$$

where n is the filter size, the filtered variables are calculated from multiple NN outputs.

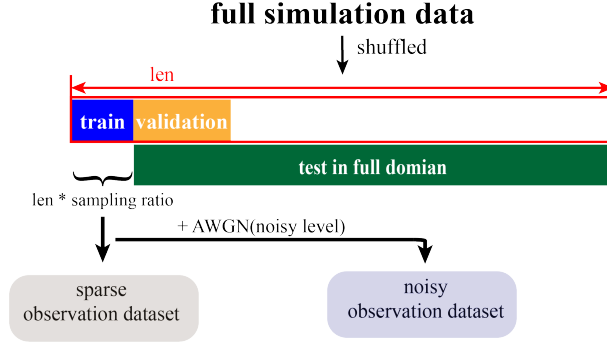


Fig. 7. The pre-processing in full simulation data. In the experiments, the training data is randomly sampled in full dataset. In sparse group, the sampling ratio is the adjustable variable. In noisy group, the noisy level is the adjustable variable.

3.3 Design of experiments

Three experiments—the cylinder flow, cell migration, and artery flow—are used to demonstrate the performance of FPDE on sparse and noisy data. In the cylinder flow case, the improvements of FPDE with simulation data are verified quantitatively; in the cell migration case, we evaluate the FPDE’s ability to correct real data when equations have missing coefficients; in the arterial flow case, we assess the performance of FPDE with inconsistent equations and observation data.

3.3.1 Simulation data of cylinder flow

To verify the improvement of FPDE under sparse and noisy training data, the sparse dataset and noise dataset are designed for the quantitative experiment. In the experiment, the sampling ratio and noise level can be controlled to quantitatively demonstrate the improvement effect of FPDE.

We designed two experiments to verify the FPDE improvements in sparsity and noise of training data. In the generation of sparse data in Group 1, the datasets are randomly sampled by the decreasing sampling ratios in Table.1. To demonstrate the NN restoration ability under various levels of data missing, seven datasets of different sizes are employed in Group 1. Obviously, the less observation it has, the more inaccuracy it produces. In Group 2, noise is added to the $[u, v, p]$ field to make training more difficult (as demonstrated in proposition 2). The ‘additive white Gaussian noise’ (AWGN), the most common noise in the noise analysis, is chosen as the artificial noise added in 2^{-10} sampled dataset. The variances of the noise in $[u, v, p]$ are jointly decided by the standard deviation in $[u, v, p]$ and the noisy rate r ($\epsilon_u = N(0, r \cdot std_u)$). Seven datasets of different noisy levels are used as the variables of Group 2 to show the flow restoration ability with the different data error levels. As anticipated, higher levels of noise result in increased inaccuracies in the restoration process.

The entire simulation data is divided into 3 parts: the training, validation, and test datasets. To test the restoration ability, the restoration outputs are plotted across the entire domain. The division is shown in figure 7.

For details of cylinder flow, data sources, and pre-processing methods, please refer to appendix B. Figure 8 is an overview of the simulation data.

Finally, experiments are conducted in two groups to evaluate the effects of sparsity and noise. The details of the two groups of datasets are presented in Table 2. For each experiment, the FPDE and the baseline model are trained in parallel to show improvements. The processes of data sampling and adding noise are also described in appendix B.

The evaluation criteria are defined in equation(s) 11. The conventional PDE model and FPDE model

The time window: $[0, 20]$, $dt = 0.1$ (the u, v, p shown is clipped at $t = 8$)

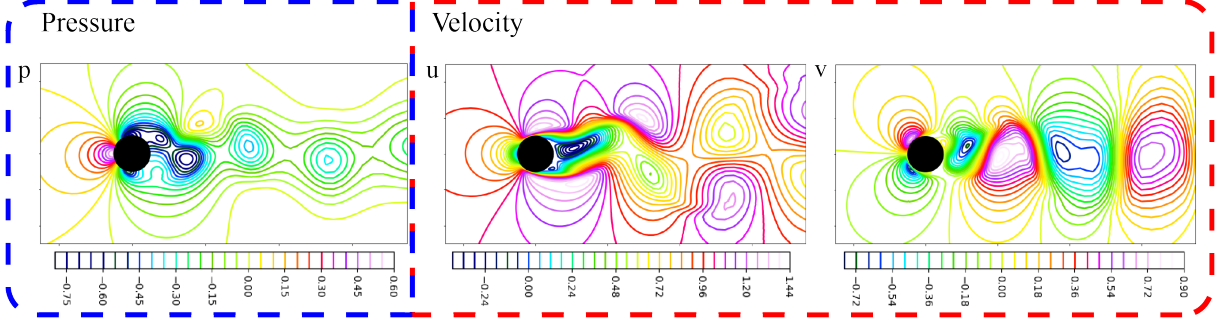


Fig. 8. The numerical simulation data of the cylinder flow problem. The training data is sampled from the original data and contaminated with noise. Similar to the boundary condition, the black circle is the cylinder wall.

Base data	Group and Data overview					
	Group 1: sparse data sampled by different sampling ratio					
full size	2^{-8}	2^{-10}	2^{-12}	2^{-13}	2^{-14}	2^{-16}
	Group 2: noisy data generated by different noisy standard deviation					
2^{-10} sampled data	$25\% \cdot std$	$50\% \cdot std$	$75\% \cdot std$	$100\% \cdot std$	$125\% \cdot std$	$150\% \cdot std$

Table 2: Summary of two groups of data. These groups of data are used to train the FPDE and conventional PDE models and validate their flow restoration abilities under sparse and noisy conditions.

are trained and tested on the same dataset.

$$\begin{aligned}
 Loss &= \frac{1}{N} \|\mathbf{y} - \hat{\mathbf{y}}\|_2 + \frac{1}{M} \left(\sum_{i=1}^3 \|e_i\|_2 \right) + \frac{1}{W} \left\| \frac{\partial^k \mathbf{y}_{IC/BC}}{\partial \mathbf{x}_{IC/BC}^k} - \frac{\partial^k \hat{\mathbf{y}}_{IC/BC}}{\partial \mathbf{x}_{IC/BC}^k} \right\| \\
 e_1 &= \frac{\partial u}{\partial t} + \left(u \frac{\partial u}{\partial x} + v \frac{\partial u}{\partial y} \right) + \frac{1}{\rho} \frac{\partial p}{\partial x} - \nu \left(\frac{\partial^2 u}{\partial x^2} + \frac{\partial^2 u}{\partial y^2} \right) \\
 e_2 &= \frac{\partial v}{\partial t} + \left(u \frac{\partial v}{\partial x} + v \frac{\partial v}{\partial y} \right) + \frac{1}{\rho} \frac{\partial p}{\partial y} - \nu \left(\frac{\partial^2 v}{\partial x^2} + \frac{\partial^2 v}{\partial y^2} \right) \\
 e_3 &= \frac{\partial u}{\partial x} + \frac{\partial v}{\partial y}
 \end{aligned} \tag{11}$$

where N, M, W represent the numbers of observation, collocation and IC/BC points in one iteration, respectively. e_1, e_2, e_3 represent the values of residual form PDE (N-S equations as example). $\frac{\partial^k}{\partial \mathbf{x}_{IC/BC}^k}$ represents the paradigm of boundary conditions in different task (e.g., $k=0 / 1$ means the Dirichlet / Neumann boundary condition).

3.3.2 Measurement data of cell migration

In this experiment, the real-world measurement data is used to demonstrate the improvement of FPDE in real-world situations. Generally, there are two difficulties when using real data in this experiment. The first challenge stems from the high noise in the observation data. In the experiments, the measurement data is mainly obtained by sensors or manual measurements, which means the data is always noisy and sparse. When the measurement data is used as observation points in physics-informed framework, it leads to conflict between data distribution and theoretical equation. The cell number C has high noise because the experimental data is automatically collected by the CV algorithm. The second challenge in this experiment is the missing coefficients in the equations. Since some coefficients of the equation are unknown, NN predicts those segments without collocation points.

The cell migration data in reproducibility of scratch assays is affected by the initial cell density in the given scratch [53]. It shows the relationship of cell distribution in scratch assays with time, space, and initial cell density. The data elucidates that when a scratch occurs, cells migrate to repair the

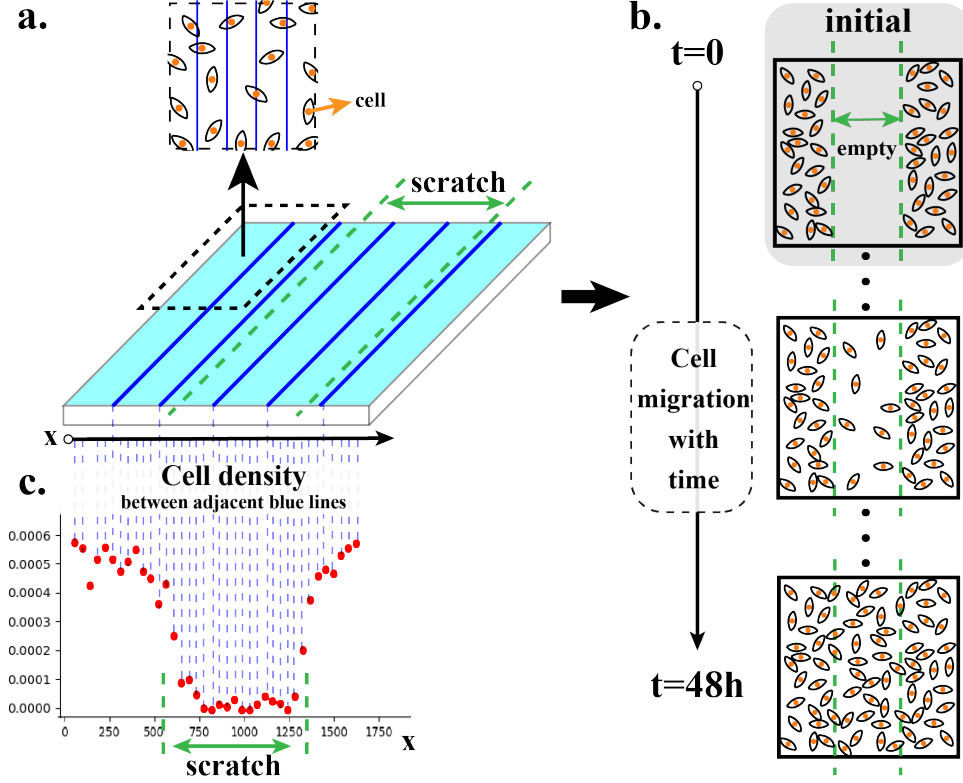


Fig. 9. The experiment of cell migration and data collection. (a) The square petri and counting method of blue lines. (b) Cells fill in the scratch by migrating. (c) Measurement data distribution.

scratch. Existing theories often use the Fisher-Kolmogorov model to describe the process of collective cell spreading, expressed as:

$$\frac{\partial C}{\partial t} = D \frac{\partial^2 C}{\partial x^2} + \lambda C \left[1 - \frac{C}{K}\right] \quad (12)$$

where the dependent variable C represents the cell concentration. K, λ and D represent the carrying capacity density, the cell diffusivity and the cell proliferation rate respectively. In this context, K, λ and D can be viewed as the coefficients decided by initial cell density (n). Because this is a variable coefficient equation, it cannot calculate the unknown PDE at any collocation points. In the experiment described in this paper, the coefficients in $n = 14,000$ and $n = 20,000$ are known. The aim is to model the $n \in (14,000, 20,000)$ interval data through the FPDE training.

The figure 9 below is a schematic diagram of the cell migration experiment. For more details on the experiment, coefficients, and dataset distribution, please refer to appendix C.

In summary, the NN models the mapping relationship ' $NN(t, x, n) \rightarrow C$ '. And the final loss function in equation(s) 4 can be written as follows (equation(s) 13). When it comes to the calculation of FPDE, the variable C is filtered first and calculated in the same form as equation(s) 13. Both the conventional PDE model and the FPDE model are trained until converged and tested on the same dataset.

$$\begin{aligned} Loss &= \frac{1}{N} \|C - \hat{C}\|_2 + \frac{1}{M} (\|e\|_2) + \frac{1}{W} \left\| \frac{\partial^k \mathbf{y}_{IC/BC}}{\partial \mathbf{x}_{IC/BC}^k} - \frac{\partial^k \hat{\mathbf{y}}_{IC/BC}}{\partial \mathbf{x}_{IC/BC}^k} \right\| \\ e &= \frac{\partial C}{\partial t} - 530.39 \frac{\partial^2 C}{\partial x^2} - 0.066C + 46.42C^2, \text{ if } n = 14,000 \\ e &= \frac{\partial C}{\partial t} - 982.26 \frac{\partial^2 C}{\partial x^2} - 0.078C + 47.65C^2, \text{ if } n = 20,000 \\ e &= 0, \text{ else} \end{aligned} \quad (13)$$

where N, M, W represent the numbers of observation, collocation and IC/BC points in one iteration, respectively. e is the residual form value of equation(s) 18. Because of the changing coefficients, e should be calculated according to three categories ($n = 14,000/20,000/else$). The constants are obtained by regression in the experiment on [54].

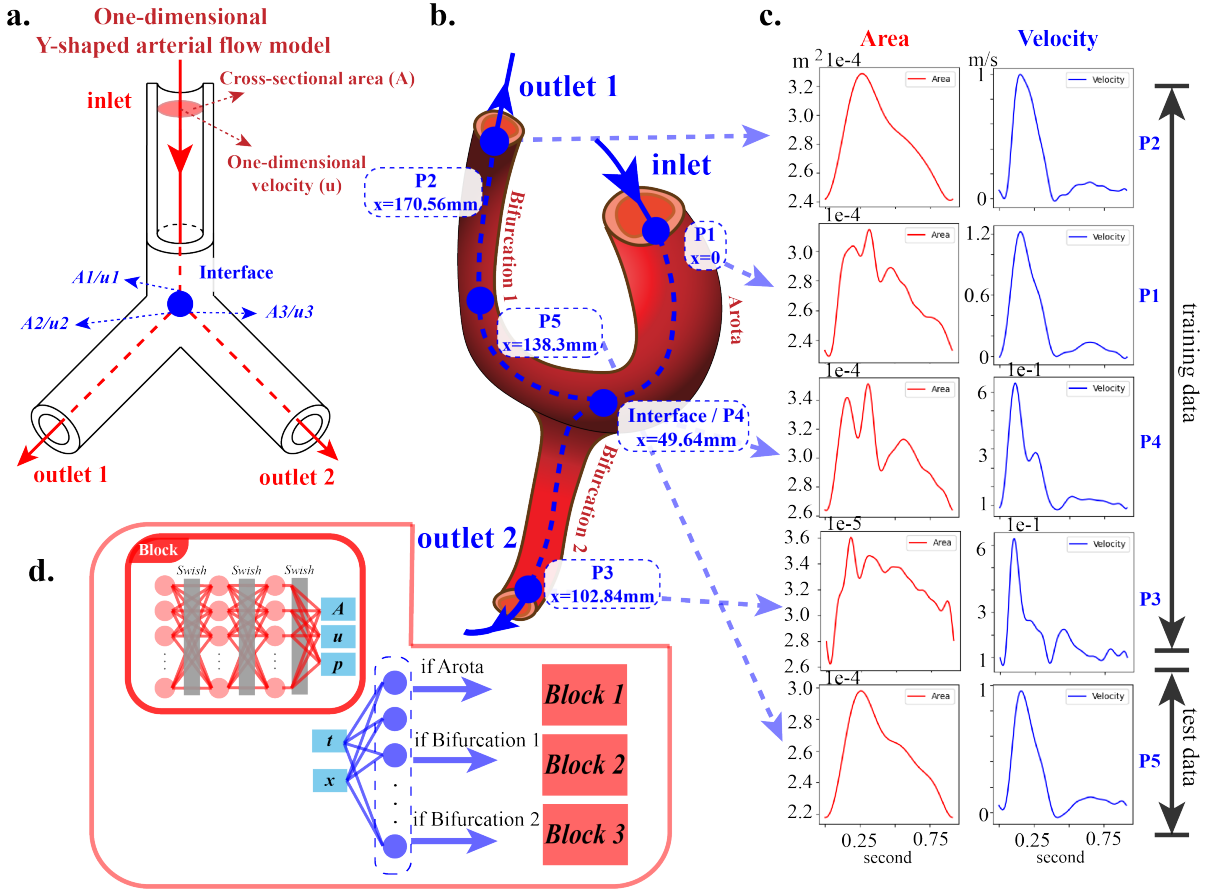


Fig. 10. The experiment of one-dimensional blood flow in the Y-shaped artery. (a) The theoretical model (including the definitions of A , A_i and *interface*). The equation(s) 14 used in the training are derived from this model. (b) The location of five measurement points and the schematic diagram of artery. (c) Overview of measurement data (area and velocity). (d) Multi-head NN to predict the velocity in different vessels.

3.3.3 Measurement data of arterial flow

When the equation is obtained through the ideal model, there are always significant disparities between the actual situation and the description of the equation. In this experiment, arterial blood flow measurements are used to compare the modeling results of FPDE and baseline with noisy data.

The data regarding arterial flow shows the velocity of blood when it flows through the arterial bifurcation [55]. The theoretical equations of velocity are shown in equation(s) 14. A is the cross-sectional area of the vessel, and u is the axial velocity. Similar to the N-S equations (equation(s) 1, ρ and p represent density and pressure, respectively), A_1 and u_1 are the cross-sectional area and velocity of the interface in the aorta. A_2, u_2 and A_3, u_3 are the area and velocity of the interface in two bifurcations. The physical relationship between the aorta and two bifurcations is shown in figure 10.a, the real-world vessel's shape is shown in figure 10.b.

$$\frac{\partial A}{\partial t} = -\frac{\partial Au}{\partial x}, \quad \frac{\partial u}{\partial t} + u \frac{\partial u}{\partial x} = -\frac{1}{\rho} \frac{\partial p}{\partial x} \quad (14)$$

$$A_1 u_1 = A_2 u_2 + A_3 u_3, \quad p_1 + \frac{\rho}{2} u_1^2 = p_2 + \frac{\rho}{2} u_2^2 = p_3 + \frac{\rho}{2} u_3^2$$

An overview of the experiment is depicted in the figure 10. Notably, a multi-head neural network is used to fit different segments of vessels. Briefly, the aim is to train the NN with measurement data from only four observation points and model the entire blood vessel.

Figure 10 illustrates the experiment of one-dimensional blood flow in the Y-shaped artery. Previous

studies modeled the velocity at the bifurcation based on an idealized Y-shaped one-dimensional vessel (shown in figure 10.a). The actual blood is not ideal, thus the measurement data always can't fit the embedding distribution in equation(s) 14 well. The conflict raised in section 2.1 affects optimization a lot. In the real experiment measuring blood flow, the schematic diagram of an artery is shown figure 10.b, with blood directions indicated by blue dotted lines. The data are measured at the five points, which are shown in figure 10.b, and the measured variables (A, u) are shown in figure 10.c. The in-vivo data is measured by the Magnetic Resonance Imaging (MRI) method in Machine learning in cardiovascular flows modeling [55]. All data (area and velocity) are measured within 850ms. Since the data is measured in an open vessel, the boundary condition is unknown in training.

In order to model the distribution ' $NN(t, x) \rightarrow (A, u, p)$ ' in three parts of vessel, we build a multi-head NN to predict the (A, u, p) in different parts separately (shown in figure 10.d). NN is trained by the data from three endpoints (points 1, 2, and 3) and the interface (point 4). The collocation points are sampled among the entire vessel as constraints. The data in point 5 is reserved for testing. During parallel training, baseline PDE is calculated directly. When calculating FPDE, the variables $y = (A, u, p)$ are filtered first and calculated in the same form as in equation(s) 15.

The final loss function in equation(s) 4 can be written as follows. Conventional PDE model and FPDE model are trained until converged and tested in same dataset.

$$\begin{aligned}
Loss &= \frac{1}{N} \|\mathbf{y} - \hat{\mathbf{y}}\|_2 + \frac{1}{M} \left(\sum_{i=1}^2 \|e_i\|_2 \right) + \frac{1}{W} \left(\sum_{i=1}^3 \|f_i\|_2 \right) \\
e_1 &= \frac{\partial A}{\partial t} + \frac{\partial Au}{\partial x}, \quad e_2 = \frac{\partial u}{\partial t} + u \frac{\partial u}{\partial x} + \frac{1}{\rho} \frac{\partial p}{\partial x} \\
f_1 &= A_1 u_1 - A_2 u_2 - A_3 u_3 \\
f_2 &= p_1 + \frac{\rho}{2} u_1^2 - p_2 - \frac{\rho}{2} u_2^2, \quad f_3 = p_1 + \frac{\rho}{2} u_1^2 - p_3 - \frac{\rho}{2} u_3^2
\end{aligned} \tag{15}$$

where N, M, W represent the numbers of observation, collocation and interface points in one iteration, respectively. e_1, e_2 represent the residual value of governing equations, f_1, f_2 represent the residual value of the interface constraints which constrain mass and energy conservation in interface.

4 Results

To ascertain the superiority of the FPDE constraint over conventional PDE constraint, the performance of the corresponding models are compared in this section via multiple experiments. For comparison, the NN output, the residual map, and the converged losses are plotted. The experimental findings offer evidence of the conflict—aligning with the hypotheses outlined in section 2.1—and corroborate that FPDE exhibits superior conflict resistance capabilities, a potential mechanism of which has been introduced in section 3.2).

4.1 The comparison between FPDE and baseline model

4.1.1 Quantitative analysis of simulation data

In the sparse data experiment, 7 pairs of converged losses are shown in the histogram of figure 11.a. The simulation data is used as the ground truth in this experiment. The x-axis of this histogram is the number of simulation data used in the training dataset, and the bar on the y-axis is the MSE on test data. The residuals between the ground truth and NN restored flow field are plotted above the loss bar, where the top is the FPDE and below is the baseline residual. According to the color map in the residual plot, a whiter color means a solution that is closer to the ground truth. In figure 11.a, the residuals of FPDE are less than baseline generally. This improvement is consistent with the losses of histogram responses.

The FPDE model exhibits superior performance under sparse observation data, a common scenario in real-world applications. For example, under the 2^{-12} sampling ratio, the MSE of the converged FPDE model is only 18% of the baseline. On average, the MSE on the converged FPDE model is 82.1% less than

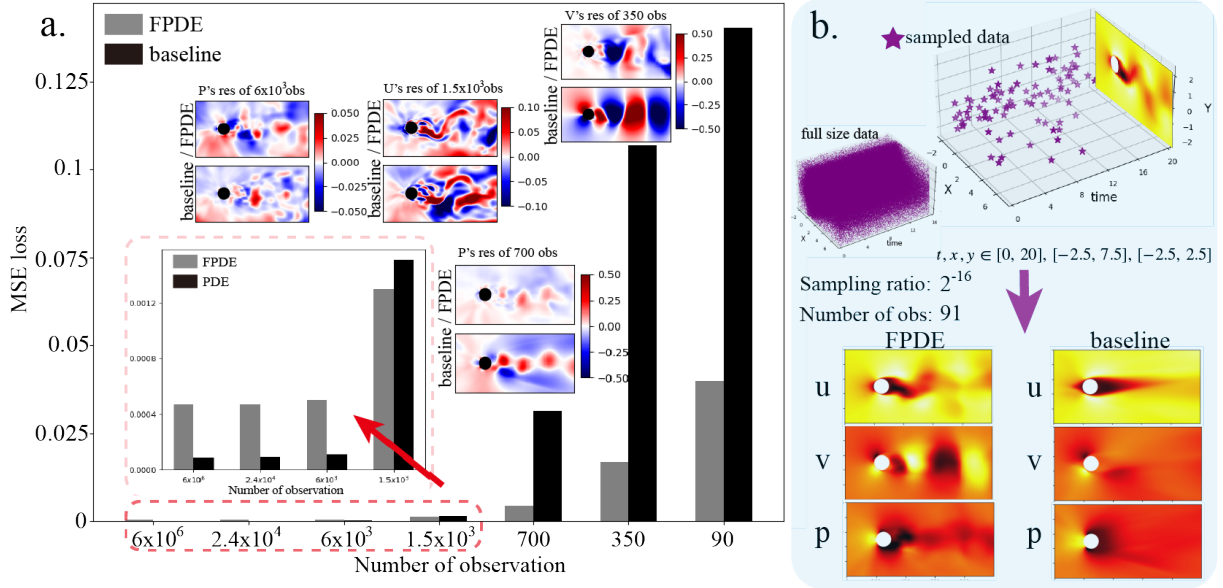


Fig. 11. The NN outputs and Mean Squared Error of the FPDE and baseline models. (a) The Mean Squared Error and the residual between the ground truth and output. This result shows the FPDE method works better with sparse observation. (b) A typical example with a 2^{-16} sampling ratio. The comparisons of NN outputs (u, v, p) are below.

the baseline model in these 7 sparse cases. However, since the data in this experiment is accurate and the observation data of the first 3 groups are enough in quantity, FPDE models show no improvements. In the magnified part in figure 11.a, the first 3 pairs of losses are close to the complete and error-free condition (i.e., case in figure 2.c). Regarding the conflict, proposition 1 posits an assumption of nearly no conflict between the PDE and data loss. However, in the context of real-world measurements, data are invariably sparse, a scenario in which FPDE models demonstrate enhanced performance.

The figure 11.b shows the typical outputs in the sparse experiment. The restoration task is similar to the pure equations solving task at the lowest sampling ratio. Using the 2^{-16} sampling ratio case as the example, the number of used simulation data points is only 91. To show the sparsity directly, the comparison between the sampled data and full-size data points is shown on the top of figure 11.b. The direct NN outputs are shown for the comparison of two models. It is obvious that the PDE solution becomes more trivial (like the example in figure 3.c). With the filter operation, FPDE model can better capture the characteristic of fluid.

In the noisy data experiment, the same kind of histogram and residuals are plotted in figure 12.a. The conflict with noisy data is shown as proposition 2, which is accurately reflected by the losses in the histogram. Under identical noisy condition, the FPDE model always converged to a lower loss. Meanwhile, the residuals also show FPDE solutions are closer to the ground truth than the baseline model at all noise levels. The figure 12.b is a typical example of this noisy group. At the highest noisy level (150% std, additive white Gaussian noise), the generation of noisy data is shown on the top of figure 12.b. Under the high-noise condition, the large-scale features disappear, and periodicity is difficult to reflect. But the FPDE model still shows better anti-noise ability than the baseline model. Only by varying the physics-informed function can the FPDE model significantly reduce the impact of outliers. On average, the MSE on the FPDE model is 62.6% less than the baseline model in these 7 noisy cases. Under the high-noise data (noisy level $> 125\%$), this number increases to 72.2%.

4.1.2 Experiment results of real-world data

The data in the cell migration case is sparse and noisy. Additionally, due to fluctuating coefficients, the NN lacks collocation points to learn PDE on the test part. Both experiment results are shown in figure 13 (initial cell number, $n = 16,000/18,000$). The predictions indicate the generalized ability of NN to learn the embedding distribution from given data. When confronted with an unknown equation, NN learns the embedding physical process (i.e., the general law of cell migration) through generalization from

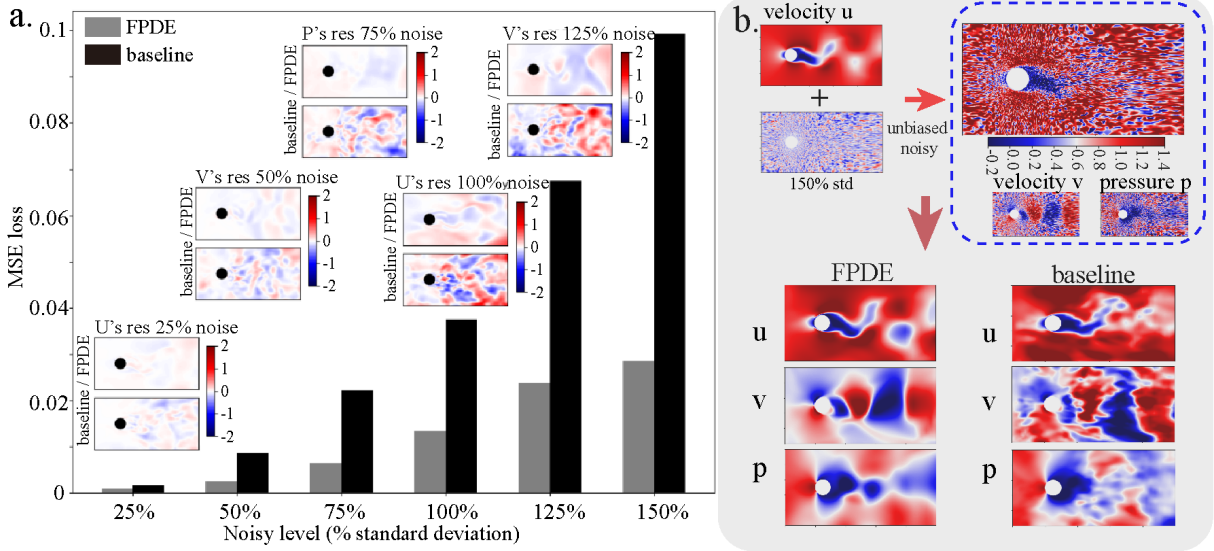


Fig. 12. The NN outputs and Mean Squared Error of the FPDE and baseline models under the noisy data condition. (a) The Mean Squared Error and residual plots. (b) The FPDE and PDE outputs under the additive white Gaussian noise with 150% standard deviation of observation data; the comparison of NN outputs is below.

given equations. In figure 13, the dots are the measurement data, and the lines are the NN predictions. Quantitatively, the MSE of normalized prediction decreased from 0.157 (baseline) to 0.121 (FPDE), a decrease of 22.9% when $n = 16,000$. When $n = 18,000$, this reduction increases to 42.9%, from 9.89×10^{-2} (baseline) to 5.64×10^{-2} (FPDE).

In the solutions of the baseline model, it is obvious that the high-noise initial data greatly affects the NN outputs. Outliers cause NN to make predictions that contradict physical laws. Although both models predict worse outcomes over time (e.g., the red lines at $t=48h$), FPDE model still has more robust results. The unreasonable solution comes due to the inability of the outliers and the physical constraints to effectively correct the prediction well. In the comparison, the FPDE model gave better predictions in the test part. The filter operation mitigates the influence of outliers and makes NN learn the embedding distribution successfully.

The difficulty in modeling the arterial flow data lies in the significant difference between the theoretical vessel model, which is used to derive the equations, and real-world vessels. The NN prediction at point 5 is tested (shown in figure 10.b) in the Y-shaped artery with measurement data. The comparison is shown in figure 14. As it demonstrated in the theoretical derivation in section 2.1, filter operations do not make NN learn the small-scale fluctuations more finely, but they do make NN model the large-scale information more precisely. On the large-scale of the velocity field, the FPDE model is less inclined to produce trivial results compared to the baseline model. Despite the absence of pressure data in the measurements, NN still gives a prediction of the pressure field through the physical constraints. Since the FPDE model is more accurate in the velocity field, it is intuitive that it has better prediction in the pressure field. Because the equations only constrain the x-direction derivative of pressure, figure 14 only shows the NN prediction of pressure individually.

4.2 Existence of ‘conflict’ in loss analysis

In the motivation part (section 2), we theoretically give the existence of conflict and how the conflict affects the co-optimization process. In our illustration, the conflict can be simply described as the ‘difference between the PDE and data loss optimization direction’. Therefore, we analyze the training losses and find the intuitive data evidence in figure 15.

The comparison between the FPDE model (up) and baseline model (down) is shown in figure 15.a and figure 15.b. Fig.15.a shows the equation loss and data loss of the FPDE and baseline model in the same experiment. In the baseline model, the equation loss is the original PDE loss. Besides, the equation loss

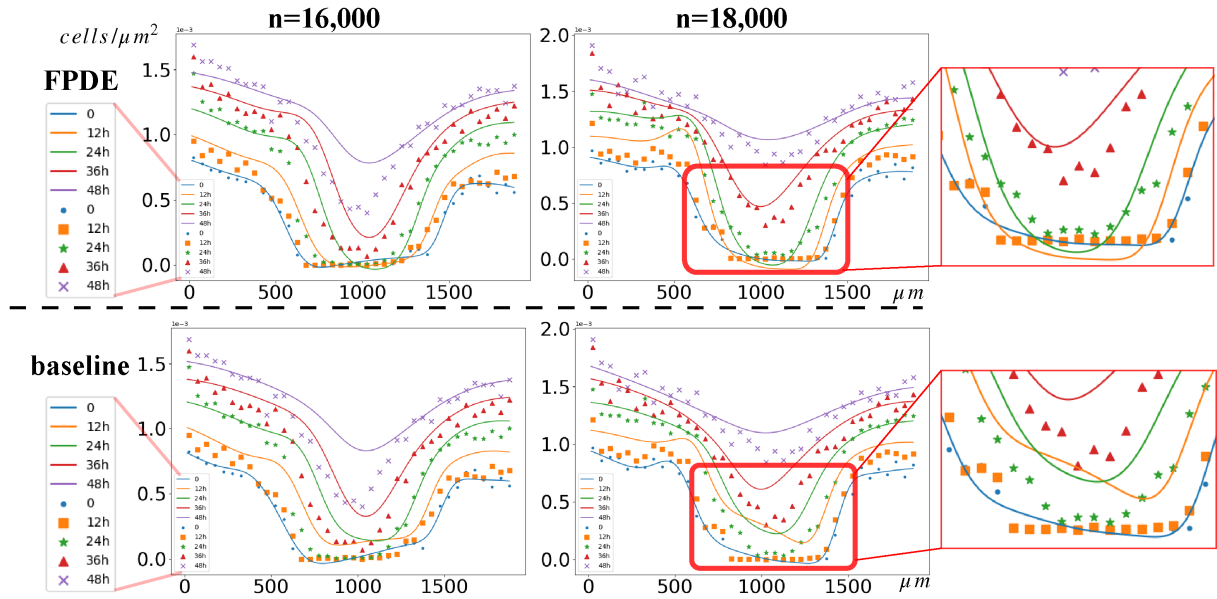


Fig. 13. Comparison in the cell migration test data (initial cell number = [16,000, 18,000]). Inside the red boxes, the difference between two outputs shows FPDE can overcome the influence of outliers better. This characteristic shows that the FPDE method has better modeling ability when faced with real, high-noise measurement data.

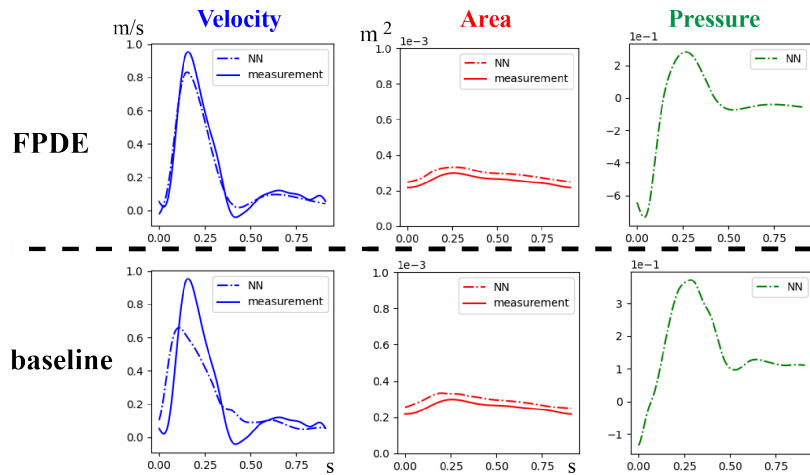


Fig. 14. Comparison in the arterial flow test data. The comparison of velocity and area at the test point is used to show the modeling ability of the FPDE and baseline models. Compare with the velocity field in baseline model, FPDE model learns better in large-scale fluctuations.

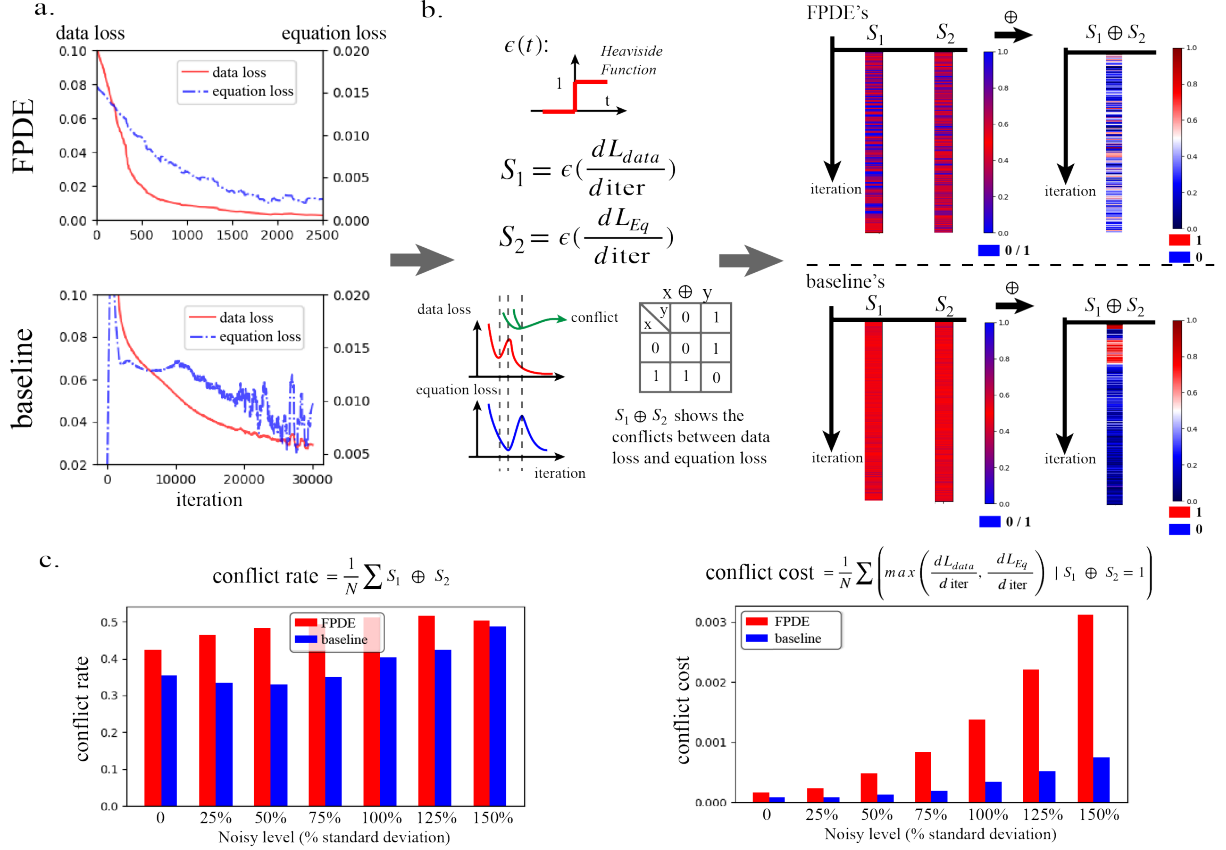


Fig. 15. Decoupling achieved by the FPDE method (reflected in training loss). (a) The PDE and data losses of two models until convergence. (b) The S and ‘exclusive OR’ color bars. In order to show the distribution of the derivative sign, the color bar is used in the after-pooling data of the original S . In the S plot, closer to red means more 0-1 oscillating and no effective gradient descent. In the $S_1 \oplus S_2$ plot, blue color indicates no conflict training process. Therefore, the effective descent in the baseline model only happened in the initial part, while the FPDE model realized decoupling throughout the whole training. (c) The definition and statistic result for each group of the conflict rate and conflict cost, which indicates higher conflict tolerance of FPDE than baseline.

is the filtered PDE loss in the FPDE model. To analyze the correlation of the loss decreasing, we defined S_1 and S_2 as the sign of the equation and data loss derivative. To facilitate the following treatments, the Heaviside function is used to replace the sign operation. Thus, the losses are transferred to the 0/1 lists S , which show the increase or decrease in this iteration. But the 0/1 list is not straightforward, so we change it to blue-red-blue color bar for better demonstration. Specifically, we first average pooling the original data of S and then map the after-pooling data to the blue-red-blue color bar (the color bar on the S left). Therefore, the S bars represent the randomness of loss as they changes by color. Because 0 and 1 represent the direction of loss change, the red color in the middle of the color bar indicates that there is oscillation in this section of the loss. Therefore, when S is in red, the training loss is oscillating, which means the optimization has no effective decrease. Conversely, when the color of the S bar approaches blue, it means the training loss tends to steadily decrease or increase in this segment.

From the color of S_1 and S_2 bar, it is obvious that the S_1 and S_2 of baseline model in figure 15.b are almost pure red. Meanwhile, the FPDE model's still have many blue segments. This indicates that the baseline model is more unstable, whereas the FPDE model can optimize effectively.

The last two bars in figure 15.b are the $S_1 \oplus S_2$ bar. S_1 and S_2 are used to show the directions of losses, thus the \oplus (exclusive OR, xor in short) can be used to show the consistency of S_1 and S_2 . If S_1 and S_2 are inconsistent ($S_1 \oplus S_2 = 1$), that means there exist conflict in the co-optimization process. The $S_1 \oplus S_2$ bar is obtained by the exclusive OR solution of the S_1 and S_2 bars, where 1 means the direction between equation and data loss is different and 0 means the same. After pooling operation, the original data is also visualized with a red-white-blue color bar, where red represents conflicts and blue represents the inverse.

The color of the baseline model in $S_1 \oplus S_2$ shows the conflicts only exist during the initial fast decline segment, and the co-optimization is avoiding the potential conflict and trapping itself in the local optimum in the following segments. Meanwhile, the color in FPDE shows the stochastic conflicts that occurred, and the co-optimization does not pay much attention to the potential conflicts, which helps it find the global optimal.

$$\begin{aligned} \text{conflict rate} &= \frac{1}{N} \sum S_1 \oplus S_2 \\ \text{conflict cost} &= \frac{1}{N} \sum \left(\max \left(\frac{dL_{data}}{dL_{train}}, \frac{dL_{pde}}{dL_{train}} \right) \mid S_1 \oplus S_2 = 1 \right) \end{aligned} \quad (16)$$

In figure 15.c, two statistical indicators are proposed to provide additional insights into the observations depicted in figure 15.b. The conflict rate is defined as the frequency of 1 in $S_1 \oplus S_2$ bar, and the conflict cost as the mean derivative of the increasing loss when the conflict happened (shown in equation(s) 16). These indicators are calculated on a group of losses with increasing noise and plot for the general comparison. Though the two indicators exhibiting an upward trend with escalating noise levels, the baseline model still prioritizes conflict avoidance in order to have a lower conflict rate and cost. The higher conflict in the FPDE reflects the decoupling process, which means the correlation between FPDE loss and data loss is decreased.

Overall, the results verify that the optimization process is effectively achieved by diminishing the correlation between the PDE and data loss. In the co-optimization process, the FPDE model can still optimize when facing higher conflict. These findings suggest that the FPDE model demonstrates greater effectiveness in addressing the challenges posed by noise and data sparsity commonly encountered in real-world measurement scenarios.

5 Conclusions

Since the data in real-world problems is often insufficient and noisy, it is necessary to improve the learning ability and robustness of the model. In other words, mitigating the reliance of the NN on data quality and quantity is a necessary prerequisite in the modeling of real-world data. One of the difficulties in the training of a physics-informed model is the conflict during the co-optimization. In this paper, we analyzed the causes of the conflict and propose the FPDE method to overcome it. The improvement of the proposed FPDE is verified in three aspects: theoretical derivation, experiments on the simulation data, and the experiments on real-world measurement data. In the comparison between the FPDE and baseline models, the proposed FPDE constraints have the following characteristics:

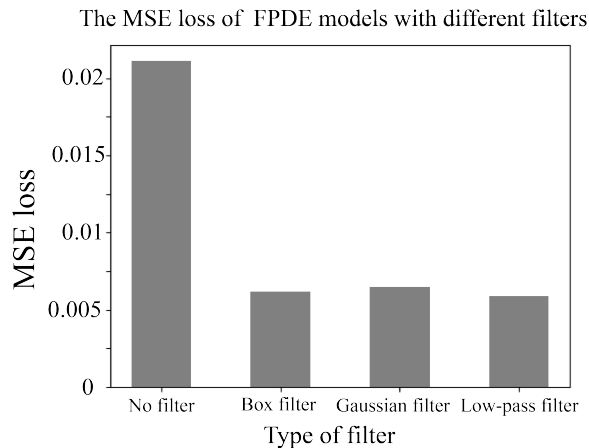


Fig. 16. The MSE of the FPDE models with different filters (including ‘no filter’). In this experiment, the chosen classic filters are the box filter, the Gaussian filter, and the low-pass filter. The conventional no-filter model is trained as the control group.

- FPDE is a general approach inspired by LES that applies to a variety of models, it is not designed for specific equations or NN architectures. As a surrogate constraint, it has good transferability in most cases.
- The FPDE method can help NN model the noisy and sparse observation data better. This improvement is important for the practical applications of the physics-informed framework.
- The FPDE method can better optimize NN when facing mismatches between the data and equations or the equation coefficients are missing.

Physics-informed methods have proliferated in recent years, and the FPDE surrogate constraint offers a notable reduction in the model’s reliance on data quality and quantity. The proposed FPDE serves as a robust constraint for PINN, exhibiting superior performance in modeling real-world problems with sparse and noisy data, which is highly desirable in practical applications. Moreover, the utilization of FPDE is straightforward, allowing for its application to other models by substituting the original equation constraints with filtered equations during the training process. This article provides an explanation of the mechanism behind the improvement of FPDE from a coupling perspective. The experimental results have shown that the FPDE loss is more prone to escaping local optima, as opposed to being tightly coupled with other losses. This decoupling mechanism not only facilitates easier optimization of FPDE but also leads to improved results, especially in scenarios with sparse and highly noisy data. In future work, additional experiments will be conducted to explore the enhancements of filters in the context of neural networks.

Appendix A Influence of filter in FPDE

A.1 Filter type

In this experiment, the FPDE models with different filters are trained with the same observation data. Thus, the accuracy of results is only determined by the type of filter. The observation data of cylinder flow with a 75% standard deviation of noise is used. For comparison, the conventional physics-informed model is trained as the control group (i.e., No filter in figure 16). The mean squared errors (MSE) of the results are shown in the figure below (figure 16).

The results illustrate that all the given filters in FPDE can improve the training result. Compared to the no-filter group, the improvements of different filters do not exhibit significant discrepancies. It is worth noting that due to the high computational cost of DNS data, only one cylinder flow dataset is utilized in the experiment. This is a typical case used in many studies (e.g., [56], [57], and [41]), which facilitates comparisons between different studies. The results in Appendix A are specific to the cylinder flow studied in the experiments and may not be directly applicable to other scenarios.

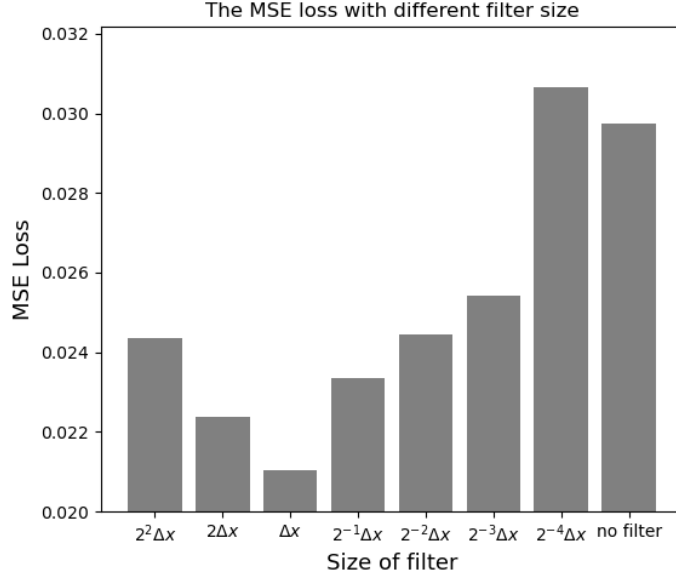


Fig. 17. The MSE of the FPDE models with different size Gaussian filters (including ‘no filter’). In this figure, Δx is used to stand for the original filter of size 0.1.

A.2 Filter size

In the previous experiments, all results were based on the filter size (Δx) of 0.1. Therefore, this experiment is designed to examine the influence of filter size on FPDE results. Ideally, when the filter size is small enough, the FPDE result should converge to the conventional PINN result. In this experiment, we used training data with a sampling ratio of 2^{-13} and $50\% \cdot std$ noise. The chosen filter is the Gaussian filter. With 10 times repeating, the average MSE loss of the converged model on the test data is shown in figure 17.

The results roughly illustrate that the improvement of FPDE will reach the optimum at an appropriate filter size. A filter size that is too large or too small will increase the MSE loss. It is worth noting that due to the statistics on the results of different fluid cases is not enough, the above conclusions can only be roughly proven on the cylinder flow dataset of this work.

Appendix B Details of cylinder flow

In this experiment, the selected computation case is the 2-dimensional cylinder flow (shown in 1.1, the background information). The cylinder flow, governed by the N-S equation, is widely studied due to its intricate characteristics. Under the small Reynolds number (Re) condition, the fluid in the cylinder flow case shows the state of Stokes flow or creeping flow [58], which can be simply linearized to the solution of the steady N-S equation. The fluid becomes turbulent as Re increases, and the velocity field shows periodicity. In the vorticity field, the famous Karman vortex street phenomenon appears [59].

The reference IC/BC (initial condition/boundary condition) conditions of the cylinder flow case are from the open resource data in the Supplementary of HFM [41], which is generated by OpenFOAM. These conditions are as follows:

$$\begin{aligned}
 u(-10, y) &= (1, 0) \\
 u\left(\frac{1}{2}\cos\theta, \frac{1}{2}\sin\theta\right) &= (0, 0), \quad \theta \in [0, 2\pi]
 \end{aligned} \tag{17}$$

where zero pressure outflow and periodicity conditions are imposed in the boundary of $[-10, 30] \cdot [-10, 10]$ simulation domain, and the simulation data is selected in $[-2.5, 7.5] \cdot [-2.5, 2.5]$ area.

This simulation data satisfied the N-S equation, which is the ideal observation data in the condition written in proposition 1. In order to do the restoration in the figure 2.b, two groups of experiments are

designed to showcase the FPDE performances under varying levels of data quality and quantity. Assume that data quality and quantity can be summarized as its noise level and sparse level, thus the simulation data of two groups is shown in Table.1. To apply the control variate method, every case in each group has two parallel models. The only difference between two parallel models is the constraint imposed on the PDE or FPDE loss. The conventional PDE guided model is used as the baseline model for this question, using the same data in both models during each pair of experiments. In order to balance the additional computational cost caused by filter operation in the FPDE model, the batch size of the baseline model is scaled up k times (where k denotes the filter size). Each model is trained for 50,000 iterations and tested in the whole selected domain ($x \in [-2.5, 7.5]$, $y \in [-2.5, 2.5]$ and $t \in [0, 16]$). Thus, the comparison reflects the improvement of the FPDE constraint compared to the conventional PDE constraint.

The training process terminates when the training loss has converged. The final loss function in equation(s) 4 can be written as follows. When training the FPDE model, the variables $y = (u, v, p)$ are filtered initially and are subsequently calculated in the same form as equation(s) 11. Each L2 error in the training process is recorded for analysis. The NN parameters are saved every 100 iterations and during iterations where the smallest validation loss is achieved.

Appendix C Details of cell migration

In equation(s) 12, the constants D, λ and K are always obtained by regression. In the experiments, these constants can be obtained by the ordinary least squares (OLS) method with measurement data. Furthermore, the simplified equations are obtained in the knowledge discovery field in equation(s) 18 [54].

$$\begin{aligned} \frac{\partial C}{\partial t} &= 530.39 \frac{\partial^2 C}{\partial x^2} + 0.066C - 46.42C^2, \quad n = 14,000 \\ \frac{\partial C}{\partial t} &= 982.26 \frac{\partial^2 C}{\partial x^2} + 0.078C - 47.65C^2, \quad n = 20,000 \end{aligned} \tag{18}$$

where n is the initial cell number. In this equation, the coefficients D, λ, K are decided by initial cell number (n), which means the initial density of cell can effect the scratch recover process.

The measurement data is generated by the cell migration experiment in square petri dishes. Over time, cells migrate and gradually fill in a scratch within the dishes, with cell densities between demarcated blue lines being quantified at 12-hour intervals. Four parallel experiments with different initial cell numbers ($n = 14,000 / 16,000 / 18,000 / 20,000$) are measured to show the effect of n on cell density. The example of actual measured data is shown in figure 9.c, which y-axis represents the cell density between adjacent blue lines ($cells/\mu m^2$) and x-axis is the location (μm). The density data in $t = 0$ is used as the initial data, while subsequent data points ($t = 12hours/24hours/36hours/48hours$) are those which the neural network (NN) is tasked with predicting.

Obviously, the measurement data is high level of noisy and conducting replicative experiments is prohibitively expensive. Moreover, the data is so sparse in the dimension of n (cell number) that it is impossible to find all coefficients for each n . In terms of the NN training, it is particularly important that the collocation points can't be selected randomly because of the unknown coefficients. Thus it only has the collocation points in $n = 14,000$ and $20,000$ flat to calculate equation(s) 18. The task is modeling the distribution of unknown equations ($n \in (14,000, 20,000)$) by the conventional PDE/FPDE method. The training data distribution is shown in figure 18.

Data and materials availability

All codes used in this manuscript are publicly available on GitHub at <https://github.com/Zzzz-Jonathan/> FPDE. Additional data related to this paper may be requested from the authors.

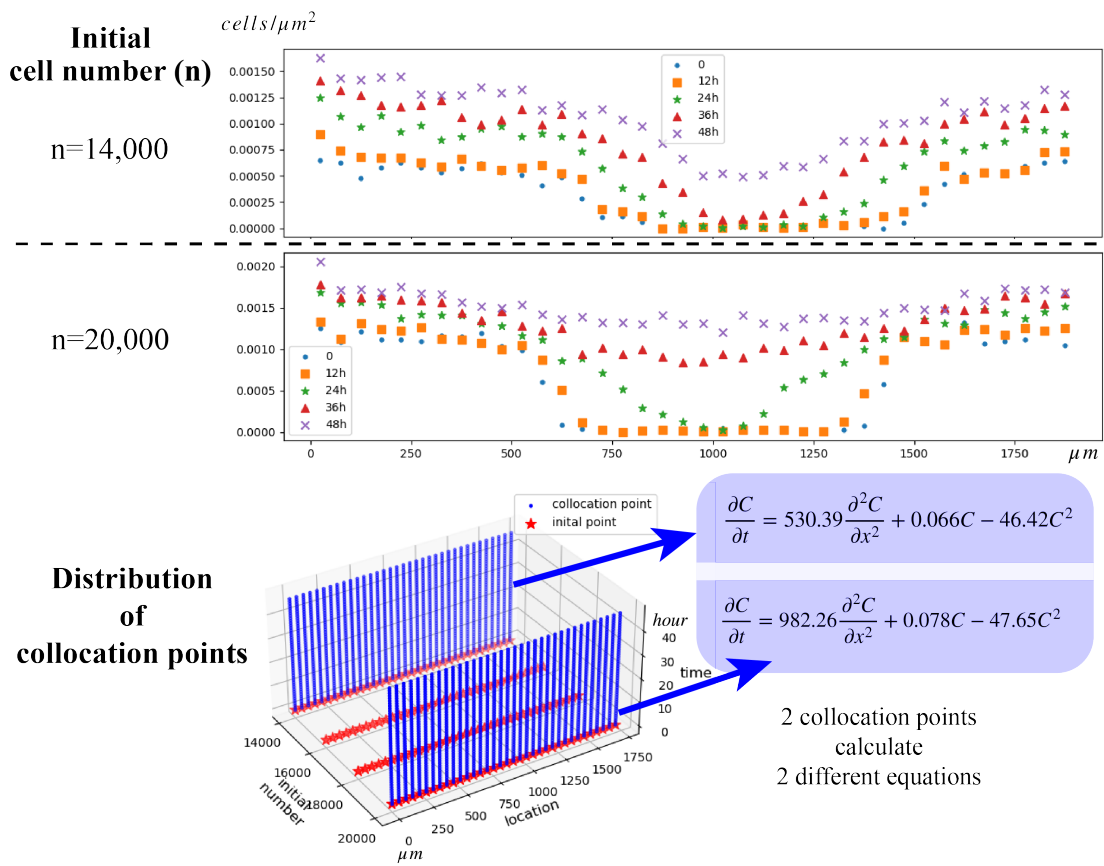


Fig. 18. The training data in cell migration modeling. The dataset's initial cell numbers are 14,000 and 20,000 for the NN training. Depending on the initial cell number, different groups fill the scratch at different speeds.

References

- [1] Maria Littmann, Katharina Selig, Liel Cohen-Lavi, Yotam Frank, Peter Hönigschmid, Evans Kataka, Anja Mösch, Kun Qian, Avihai Ron, Sebastian Schmid, et al. Validity of machine learning in biology and medicine increased through collaborations across fields of expertise. *Nature Machine Intelligence*, 2(1):18–24, 2020.
- [2] T DebRoy, T Mukherjee, HL Wei, JW Elmer, and JO Milewski. Metallurgy, mechanistic models and machine learning in metal printing. *Nature Reviews Materials*, 6(1):48–68, 2021.
- [3] John W Goodell, Satish Kumar, Weng Marc Lim, and Debidutta Pattnaik. Artificial intelligence and machine learning in finance: Identifying foundations, themes, and research clusters from bibliometric analysis. *Journal of Behavioral and Experimental Finance*, 32:100577, 2021.
- [4] Congyu Wang and Kaiping Peng. Ai experience predicts identification with humankind. *Behavioral Sciences*, 13(2):89, 2023.
- [5] David Vernon. *Machine vision: Automated visual inspection and robot vision*. Prentice-Hall, Inc., 1991.
- [6] Ivan A Sag, Timothy Baldwin, Francis Bond, Ann Copestake, and Dan Flickinger. Multiword expressions: A pain in the neck for nlp. In *International conference on intelligent text processing and computational linguistics*, pages 1–15. Springer, 2002.
- [7] Zongyi Li, Nikola Kovachki, Kamyar Aizzadenesheli, Burigede Liu, Kaushik Bhattacharya, Andrew Stuart, and Anima Anandkumar. Fourier neural operator for parametric partial differential equations. *arXiv preprint arXiv:2010.08895*, 2020.
- [8] Zelong Yuan, Chenyue Xie, and Jianchun Wang. Deconvolutional artificial neural network models for large eddy simulation of turbulence. *Physics of Fluids*, 32(11):115106, 2020.
- [9] Tianyi Li, Michele Buzzicotti, Luca Biferale, Fabio Bonaccorso, Shiyi Chen, and Mingping Wan. Data reconstruction of turbulent flows with gappy pod, extended pod and generative adversarial networks. *arXiv preprint arXiv:2210.11921*, 2022.
- [10] Sebastian Ruder. An overview of gradient descent optimization algorithms. *arXiv preprint arXiv:1609.04747*, 2016.
- [11] Kunihiko Fukushima and Sei Miyake. Neocognitron: A self-organizing neural network model for a mechanism of visual pattern recognition. In *Competition and cooperation in neural nets*, pages 267–285. Springer, 1982.
- [12] Han Zhang, Ian Goodfellow, Dimitris Metaxas, and Augustus Odena. Self-attention generative adversarial networks. In *International conference on machine learning*, pages 7354–7363. PMLR, 2019.
- [13] Maziar Raissi, Paris Perdikaris, and George E Karniadakis. Physics-informed neural networks: A deep learning framework for solving forward and inverse problems involving nonlinear partial differential equations. *Journal of Computational physics*, 378:686–707, 2019.
- [14] Lu Lu, Xuhui Meng, Zhiping Mao, and George Em Karniadakis. Deepxde: A deep learning library for solving differential equations. *SIAM Review*, 63(1):208–228, 2021.
- [15] Mengge Du, Yuntian Chen, and Dongxiao Zhang. Autoke: An automatic knowledge embedding framework for scientific machine learning. *arXiv preprint arXiv:2205.05390*, 2022.
- [16] Feiyu Chen, David Sondak, Pavlos Protopapas, Marios Mattheakis, Shuheng Liu, Devansh Agarwal, and Marco Di Giovanni. Neurodiffee: A python package for solving differential equations with neural networks. *Journal of Open Source Software*, 5(46):1931, 2020.
- [17] Yuntian Chen and Dongxiao Zhang. Integration of knowledge and data in machine learning. *arXiv preprint arXiv:2202.10337*, 2022.
- [18] Samuel H Rudy, Steven L Brunton, Joshua L Proctor, and J Nathan Kutz. Data-driven discovery of partial differential equations. *Science advances*, 3(4):e1602614, 2017.

- [19] Hao Xu, Haibin Chang, and Dongxiao Zhang. Dl-pde: Deep-learning based data-driven discovery of partial differential equations from discrete and noisy data. *arXiv preprint arXiv:1908.04463*, 2019.
- [20] Yuntian Chen, Yingtao Luo, Qiang Liu, Hao Xu, and Dongxiao Zhang. Any equation is a forest: Symbolic genetic algorithm for discovering open-form partial differential equations (sga-pde). *arXiv preprint arXiv:2106.11927*, 2021.
- [21] Karthik Duraisamy, Gianluca Iaccarino, and Heng Xiao. Turbulence modeling in the age of data. *Annual review of fluid mechanics*, 51:357–377, 2019.
- [22] Patricio Clark Di Leoni, Karuna Agarwal, Tamer A Zaki, Charles Meneveau, and Joseph Katz. Reconstructing turbulent velocity and pressure fields from under-resolved noisy particle tracks using physics-informed neural networks. *Experiments in Fluids*, 64(5):95, 2023.
- [23] Yifan Du, Mengze Wang, and Tamer A Zaki. State estimation in minimal turbulent channel flow: a comparative study of 4dvar and pinn. *International Journal of Heat and Fluid Flow*, 99:109073, 2023.
- [24] Karthik Duraisamy. Perspectives on machine learning-augmented reynolds-averaged and large eddy simulation models of turbulence. *Physical Review Fluids*, 6(5):050504, 2021.
- [25] George S Misyris, Andreas Venzke, and Spyros Chatzivasiladiadis. Physics-informed neural networks for power systems. In *2020 IEEE Power & Energy Society General Meeting (PESGM)*, pages 1–5. IEEE, 2020.
- [26] Yuntian Chen, Dou Huang, Dongxiao Zhang, Junsheng Zeng, Nanzhe Wang, Haoran Zhang, and Jinyue Yan. Theory-guided hard constraint projection (hcp): A knowledge-based data-driven scientific machine learning method. *Journal of Computational Physics*, 445:110624, 2021.
- [27] Adil Rasheed, Omer San, and Trond Kvamsdal. Digital twin: Values, challenges and enablers from a modeling perspective. *Ieee Access*, 8:21980–22012, 2020.
- [28] Romit Maulik, Omer San, Adil Rasheed, and Prakash Vedula. Subgrid modelling for two-dimensional turbulence using neural networks. *Journal of Fluid Mechanics*, 858:122–144, 2019.
- [29] Khemraj Shukla, Patricio Clark Di Leoni, James Blackshire, Daniel Sparkman, and George Em Karniadakis. Physics-informed neural network for ultrasound nondestructive quantification of surface breaking cracks. *Journal of Nondestructive Evaluation*, 39(3):1–20, 2020.
- [30] Chulin Wang, Eloisa Bentivegna, Wang Zhou, Levente Klein, and Bruce Elmeegreen. Physics-informed neural network super resolution for advection-diffusion models. *arXiv preprint arXiv:2011.02519*, 2020.
- [31] Shengze Cai, Zhicheng Wang, Frederik Fuest, Young Jin Jeon, Callum Gray, and George Em Karniadakis. Flow over an espresso cup: inferring 3-d velocity and pressure fields from tomographic background oriented schlieren via physics-informed neural networks. *Journal of Fluid Mechanics*, 915:A102, 2021.
- [32] Hongping Wang, Yi Liu, and Shizhao Wang. Dense velocity reconstruction from particle image velocimetry/particle tracking velocimetry using a physics-informed neural network. *Physics of Fluids*, 34(1), 2022.
- [33] Gazi Hasanuzzaman, Hamidreza Eivazi, Sebastian Merbold, Christoph Egbers, and Ricardo Vinuesa. Enhancement of piv measurements via physics-informed neural networks. *Measurement Science and Technology*, 34(4):044002, 2023.
- [34] Ke Zhou, Jiaqi Li, Jiarong Hong, and Samuel J Grauer. Stochastic particle advection velocimetry (spav): theory, simulations, and proof-of-concept experiments. *Measurement Science and Technology*, 34(6):065302, 2023.
- [35] Nanzhe Wang, Dongxiao Zhang, Haibin Chang, and Heng Li. Deep learning of subsurface flow via theory-guided neural network. *Journal of Hydrology*, 584:124700, 2020.
- [36] Eric J Hartman, James D Keeler, and Jacek M Kowalski. Layered neural networks with gaussian hidden units as universal approximations. *Neural computation*, 2(2):210–215, 1990.
- [37] Roger Temam. *Navier–Stokes equations and nonlinear functional analysis*. SIAM, 1995.

- [38] CY Wang. Exact solutions of the steady-state navier-stokes equations. *Annual Review of Fluid Mechanics*, 23(1):159–177, 1991.
- [39] Roland Glowinski and Olivier Pironneau. Finite element methods for navier-stokes equations. *Annual review of fluid mechanics*, 24(1):167–204, 1992.
- [40] Michael Schäfer, Stefan Turek, Franz Durst, Egon Krause, and Rolf Rannacher. Benchmark computations of laminar flow around a cylinder. In *Flow simulation with high-performance computers II*, pages 547–566. Springer, 1996.
- [41] Maziar Raissi, Alireza Yazdani, and George Em Karniadakis. Hidden fluid mechanics: Learning velocity and pressure fields from flow visualizations. *Science*, 367(6481):1026–1030, 2020.
- [42] Ian J Goodfellow, Oriol Vinyals, and Andrew M Saxe. Qualitatively characterizing neural network optimization problems. *arXiv preprint arXiv:1412.6544*, 2014.
- [43] Joseph Smagorinsky. General circulation experiments with the primitive equations: I. the basic experiment. *Monthly weather review*, 91(3):99–164, 1963.
- [44] Sifan Wang, Yujun Teng, and Paris Perdikaris. Understanding and mitigating gradient flow pathologies in physics-informed neural networks. *SIAM Journal on Scientific Computing*, 43(5):A3055–A3081, 2021.
- [45] Sifan Wang, Xinling Yu, and Paris Perdikaris. When and why pinns fail to train: A neural tangent kernel perspective. *Journal of Computational Physics*, 449:110768, 2022.
- [46] Salvatore Cuomo, Vincenzo Schiano Di Cola, Fabio Giampaolo, Gianluigi Rozza, Maziar Raissi, and Francesco Piccialli. Scientific machine learning through physics-informed neural networks: Where we are and what’s next. *Journal of Scientific Computing*, 92(3):88, 2022.
- [47] Miao Rong, Dongxiao Zhang, and Nanzhe Wang. A lagrangian dual-based theory-guided deep neural network. *Complex & Intelligent Systems*, 8(6):4849–4862, 2022.
- [48] Shengze Cai, Zhicheng Wang, Sifan Wang, Paris Perdikaris, and George Em Karniadakis. Physics-informed neural networks for heat transfer problems. *Journal of Heat Transfer*, 143(6):060801, 2021.
- [49] Somdatta Goswami, Cosmin Anitescu, Souvik Chakraborty, and Timon Rabczuk. Transfer learning enhanced physics informed neural network for phase-field modeling of fracture. *Theoretical and Applied Fracture Mechanics*, 106:102447, 2020.
- [50] Ugo Piomelli. Large-eddy simulation: achievements and challenges. *Progress in aerospace sciences*, 35(4):335–362, 1999.
- [51] GX Cui, CX Xu, and ZS Zhang. Progress in large eddy simulation of turbulent flows. *Acta Aerodynamica Sinica*, 22(2):121–129, 2004.
- [52] John G Saw, Mark CK Yang, and Tse Chin Mo. Chebyshev inequality with estimated mean and variance. *The American Statistician*, 38(2):130–132, 1984.
- [53] Wang Jin, Esha T Shah, Catherine J Penington, Scott W McCue, Lisa K Chopin, and Matthew J Simpson. Reproducibility of scratch assays is affected by the initial degree of confluence: experiments, modelling and model selection. *Journal of theoretical biology*, 390:136–145, 2016.
- [54] Zhao Chen, Yang Liu, and Hao Sun. Physics-informed learning of governing equations from scarce data. *Nature communications*, 12(1):1–13, 2021.
- [55] Georgios Kissas, Yibo Yang, Eileen Hwuang, Walter R Witschey, John A Detre, and Paris Perdikaris. Machine learning in cardiovascular flows modeling: Predicting arterial blood pressure from non-invasive 4d flow mri data using physics-informed neural networks. *Computer Methods in Applied Mechanics and Engineering*, 358:112623, 2020.
- [56] Chen Cheng, Hao Meng, Yong-Zheng Li, and Guang-Tao Zhang. Deep learning based on pinn for solving 2 dof vortex induced vibration of cylinder. *Ocean Engineering*, 240:109932, 2021.
- [57] Chengping Rao, Hao Sun, and Yang Liu. Physics-informed deep learning for incompressible laminar flows. *Theoretical and Applied Mechanics Letters*, 10(3):207–212, 2020.
- [58] MD Chilcott and John M Rallison. Creeping flow of dilute polymer solutions past cylinders and spheres. *Journal of Non-Newtonian Fluid Mechanics*, 29:381–432, 1988.
- [59] R Wille. Karman vortex streets. *Advances in Applied Mechanics*, 6:273–287, 1960.